Calorific Analysis of the Mechanical Response of Granular Materials Composed of Ellipsoidal Rubbery Particles

Kunanon Jongchansitto, Pawarut Jongchansitto, Xavier Balandraud, Itthichai Preechawuttipong, Jean-Benoit Le Cam, F. Blanchet, Benoît Blaysat, Michel Grédiac

Calorific Analysis of the Mechanical Response of Granular Materials Composed of Ellipsoidal Rubbery Particles

K. Jongchansitto[1,2], P. Jongchansitto[1], X. Balandraud[2], I. Preechawuttipong[1], J.-B. Le Cam[3], F. Blanchet[3], B. Blaysat[2], M. Grédiac[2]

Background Infrared thermography (IRT) techniques and full-field deformation calorimetry approaches have profoundly impacted the experimental mechanics community. The way in which granular materials are tested is currently excluded from this trend, as evidenced by the small number of papers in the literature mentioning the use of thermographic cameras.

Objective The objective of this work was to perform a thermomechanical analysis of soft granular systems by distinguishing temperature changes associated with thermoelastic coupling (TEC) and mechanical dissipation (MD). **Methods** Cyclic confined compression was applied to different granular systems consisting of ellipsoidal cross-section cylinders made of thermoplastic polyurethane. The temperatures measured using IRT were processed to identify the heat associated with TEC and MD, based on considerations of adiabaticity and thermodynamic cycle completion. Various granular configurations and spatial resolutions of the thermal maps were compared.

Results Strong TEC is revealed around the contact areas between all particles, which can be explained by stress concentrations. Strong MD is found around specific contacts, as well as within some particles, which can be explained by viscosity and friction. TEC data was processed for a granular system comprised of about 600 interparticle contacts, providing statistical information.

Conclusions TEC appears to be a strong coupling in the sense that its intensity is much higher than that of the MD. It is shown that IRT provides valuable information at the local scale, namely the signature of reversible (TEC) and irreversible (MD) mechanical phenomena, both at the interparticle contacts and inside the particles.

Keywords Discrete material · Infrared thermography · Mechanical dissipation · Thermoelastic coupling · Thermoplastic polyurethane

Nomenclature

DIC	Digital image correlation
IR	Infrared
MD	Mechanical dissipation
PDF	Probability density function
POM	Polyoxymethylene
TEC	Thermoelastic coupling
TPU	Thermoplastic polyurethane
TSA	Thermoelastic stress analysis
θ	Temperature change (with respect to the beginning of the test)
$\theta_{\text{half}}(\#k)$	Temperature change at the middle of the k^{th} cycle, when the force level is maximum
$\theta_{\text{end}}(\#k)$	Temperature change at the end of the k^{th} cycle, when the force level is minimum
$Q_{\text{TEC}}(\#k)$	Heat density due to TEC over half of the k^{th} cycle, during the loading phase
$Q_{\text{MD}}(\#k)$	Heat density due to MD over the k^{th} cycle (loading + unloading)
$Q_{\text{MD}}(\text{stab})$	Mean heat density per cycle due to MD in the stabilized regime

✉ P. Jongchansitto
pawarut.j@cmu.ac.th

[1] Department of Mechanical Engineering, Faculty of Engineering, Chiang Mai University, Chiang Mai 50200, Thailand

[2] Université Clermont Auvergne, Clermont Auvergne INP, CNRS, Institut Pascal, 63000 Clermont-Ferrand, France

[3] Institut de Physique, Université de Rennes 1, 35042 Rennes Cedex, France

Introduction

Granular materials can be defined as sets of small solid particles. Their mechanical behavior is different from that of classical continuous solids, liquids and gases [1, 2]. Like solids, they can withstand deformation; like liquids, they can flow; like gases, they exhibit compressibility [3]. Their macroscopic mechanical response is governed by the interparticle contact forces which act at the local scale. They can be composed of particles of various sizes, shapes and base materials, which makes it difficult to define general mechanical behavior laws. Over the last decades, numerical simulations relying on molecular dynamics or discrete element methods have widely been applied to study the influence of parameters such as particle shape, density, level of polydispersity, contact stiffness or other parameters defining friction conditions [4]. Some full-field experimental techniques are also available. For measurements in the bulk, X-ray tomography [5] and the carbon paper method [6] can be mentioned. For surface measurements, a classical way is to consider two-dimensional (2D) granular systems composed of cylinders placed in parallel. Such systems are named *Schneebeli materials* [7]. In this case, the mechanical load is applied perpendicularly to the cylinders' axis while a camera acquires images of the free ends of the cylinders. Particle image velocimetry (PIV) and digital image correlation (DIC) processing have widely been used to analyze the rigid-body motion of particles and the corresponding strain patterns of such granular assemblies [8–12]. In particular, the pioneering works of Calvetti [8] and Misra [9] identified deformation patterns by using wood, aluminum and plastic rods under a variety of two-dimensional loads (compression, shear, compression/shear; displacement-controlled boundaries, mixed stress-controlled/displacement-controlled boundaries). DIC has also been applied to measure the strain components on the surface of each particle [13–16]. Shear stress fields have also been deduced by photoelasticimetry by using particles made of birefringent transparent materials [17–19]. Obtaining information about the "network" of strains or stresses in granular materials is one of the objectives of the experimental studies presented in the literature.

Most of these experimental studies involve rigid particles. The study of granular materials containing soft particles has only been addressed very recently [4, 20], despite the fact that they are commonly found in nature and in industry (*e.g.* pharmaceutical and food fields). This can be explained by the experimental difficulties associated with the large displacements/strains of the particles, which complicate the data processing and analysis. Experimental studies are still rare in the literature. Let us mention the study of the compressive behavior of 2D bidisperse granular assemblies made of soft and hard grains using DIC in Ref [21]. It can be noted that numerical studies are also scarce: let us mention Ref [22], presenting a coupling of discrete and finite element methods carried out for highly deformable particle assemblies.

Infrared (IR) thermography has deeply impacted the experimental mechanics community over the last decades. Basically, the approach consists of analyzing the thermal response of a material subjected to a mechanical loading at constant room temperature. Under some mild assumptions, it is possible to assess the heat produced or absorbed by the material due to the change in its mechanical state [23]. Under cyclic loading, it is possible to deduce the field of hydrostatic stress amplitudes from the temperature oscillations using the so-called Thermoelastic Stress Analysis (TSA) technique [24]. The processing relies on thermoelastic coupling, which exists in all materials featuring a non-null thermal expansion coefficient. Other approaches enable the identification of the calorific signature beyond thermoelastic coupling, for example related to plasticity, fatigue damage, viscosity, solid-solid phase change or cracking, depending on the type of material and loading conditions. More generally, the use of IR thermography and the framework of the thermodynamics of irreversible processes [25, 26] makes it possible to perform full-field "deformation calorimetry". IR thermography techniques applied to mechanics of materials are now mature. They have profoundly impacted the experimental mechanics community in recent years. The way granular materials are tested is currently absent from this trend, as evidenced by the small number of papers published in the literature mentioning the use of IR cameras. These papers are briefly discussed below.

In the 80s, Luong applied vibrothermography to sand, revealing self-heating caused by the friction between grains during cyclic loading [27, 28]. The dissipative behavior of sands and soils was then discussed in the 2000s. For instance, it was shown in Refs [29, 30] that thermography allows real-time observations of heat patterns produced by the dissipation of energy. Self-heating of more than 5 °C was measured, which experimentally evidenced the presence of strong dissipative effects in sands under vibration. In these studies, the size of the grains was much smaller than the size of the IR pixel projected onto the measurement area, thus enabling "continuous" thermal fields to be obtained for granular samples with a large number of particles. In previous studies by the present authors, thermographic measurements were first performed on Schneebeli materials made with circular cross-section cylinders. In 2014, granular systems with about 1200 rigid particles made of polyoxymethylene (POM) and high-density polyethylene (HDPE) were analyzed by using TSA data averaged over each particle [31]. Temperature oscillations of more than 0.1 °C in amplitude were measured under cyclic mechanical loading at 3 Hz. Note that the use of rapid and repeated cycles was required to obtain hydrostatic stress distributions with sufficient sensitivity. The latter was about 0.015 °C/MPa and 0.026 °C/MPa for POM and HDPE

respectively. Then, in 2015, TSA was applied to granular systems made of a few hundred POM particles in order to analyze localizations within them [32]. It enabled us to evidence hydrostatic stress "paths" within the particles from temperature oscillations up to about 0.2 °C in amplitude. Because of the need for numerous and rapid mechanical cycles (to ultimately obtain only a low thermal response), the suitability of the methodology was questioned in 2018 in Ref [33]. In this work, rigid and soft particles made of POM and thermoplastic polyurethane (TPU), respectively, were mixed. It was found that temperature variations of more than 0.8 °C could be obtained in the soft particles without the need to average the values over several cycles. Some comments can be made here regarding thermoelastic couplings, depending on the type of elasticity (see page 310 of Ref [34] for more details about the comparison between the two types of elasticity):

- TSA relies on the thermal sensitivity of the volume change in materials featuring *energetic* elasticity (these materials are sometimes called isentropic). This sensitivity, expressed by the thermal expansion coefficient, is low for rigid materials. TSA provides maps of hydrostatic stress amplitude under cyclic loading. The method requires sufficiently high loading frequencies (to maximize the number of cycles over short times) and sufficiently high stress levels (when possible) to reach a sufficient thermal signal-to-noise ratio.
- Elastomeric materials feature *entropic* elasticity. Deformation-induced temperature variations in rubbers were initially discussed in the pioneering studies of Gough [35] and Joule [36] in the nineteenth century. The temperature changes caused by entropic elasticity are much higher than those resulting from energetic elasticity. In fact, both types of thermoelastic coupling exist in rubber-like materials, but that caused by entropic elasticity is rapidly predominant compared to that caused by energetic elasticity when the strain level increases [37].

In this context, the objective of the present study is to take advantage of the strong thermal signature of entropic elasticity to analyze the thermomechanical response of granular materials entirely composed of elastomeric particles. Furthermore, studying soft granular systems is a topical issue (see Refs [4, 20]) for which there is a lack of full-field experimental measurements. Elliptical shapes for the particles are considered in the present study as step towards more complex geometries in the future, to progressively approach the particle shapes of real granular media. Performing a statistical analysis is another challenge for this study, through an experiment on a granular system with about 100 particles and about 600 interparticle contacts. Note that we did not seek to identify stress fields, as was done in Ref [32] by TSA in the case of particles with energetic elasticity. The identification of stresses in elastomeric materials using IR thermography is a topic which is not considered here.

The paper is organized as follows. The second section presents the granular materials and the experimental devices used in the study. The third section presents some preliminary observations for a given test in order to illustrate a typical thermal response. The fourth section describes the procedure employed to extract calorific data from thermal measurements obtained by IR thermography. The fifth section aims at analyzing small-size granular systems (about 15 particles) at the local scale, using various spatial resolutions for comparison purposes. In order to approach real granular media, the sixth section is devoted to a statistical analysis on a larger granular system comprising about 100 particles. Concluding remarks close the paper.

Material and Methods

Particle Preparation

Figure 1 illustrates the preparation of the TPU particles employed in the experiments. Particles were prepared from a commercial biresin grade from Axson Technologies, composed of U1419-I1 isocyanate and U1458 polyol. To manufacture cylinders with elliptical cross-sections, the biresin was mixed and poured in molds. A vacuum chamber was used to remove bubbles from the mixture (see Fig. 1(a)). Twenty minutes were necessary for the complete solidification of the cylinders (see Fig. 1(b)), all of which were 26 mm long. Three dimensions were considered for the cross-sections, simply referred to as "small", "medium" and "large" in the following

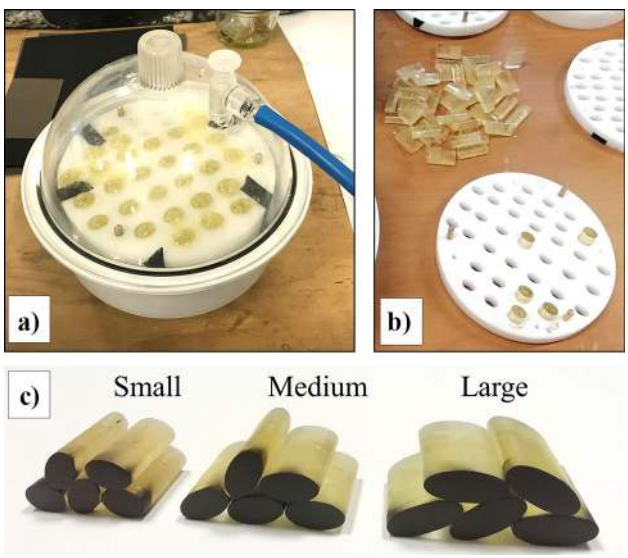

Fig. 1 Material elaboration and elliptical particles

of the paper for the sake of simplicity, see Fig. 1(c). The cylinders differed in the length of the major axis of the elliptical section, which was equal to 15 mm, 18 mm and 22.5 mm, respectively. The length of the minor axis was the same for all the particles: 10 mm. The cylinders were slightly polished on one end and coated with a thin matte black paint to maximize the thermal emissivity of the surface. Finally, two material parameters are reported here for the subsequent calorific analysis of the thermal response of the granular systems made from the particles. The density of TPU was 1,040 kg/m^3 according to the datasheet of the supplier. A value of 1,700 J/(kg·K) was considered for the specific heat [38].

Experimental Setup

Figure 2 shows the two types of thermomechanical setup used during this study. They differ in the size of the rectangular metal frame receiving the particles for confined compressive loads: 50 mm and 150 mm in width (see Fig. 2(a), (c) respectively). A pusher was employed to apply a vertical load at the top of the granular systems thanks to a linear actuator. Two uniaxial testing machines were used: an Intron ElectroPuls E3000 machine and a Zwick/Roell Zmart Pro machine. The former allows cyclic loadings with a maximum compression force of 5 kN, enabling us to study the influence of the loading rate on small granular systems (about 15 particles). The latter allows quasi-static loadings up to 15 kN, enabling us to study the influence of the loading level on a large granular system (about 100 particles).

As mentioned above, all the particles were painted in black to maximize their thermal emissivity. As can be seen in the pictures, the metallic frames were also spray-painted to limit parasitic reflections in the IR range (see Fig. 2(d)). In addition, thick black fabrics were placed all around the granular systems (see Fig. 2(b)). A cardboard tunnel (not visible in the pictures) was also placed from the IR camera to the granular material to minimize parasitic radiations caused by the close environment.

Mechanical Loading and Thermal Measurement

The granular systems were subjected to force-controlled cyclic loadings with a triangular profile. In all the tests, the minimum vertical compression force was set at 10% of the maximum force to avoid any loss of contact during unloading. Various tests were performed. Table 1 gives the list of the tests discussed in detail in the paper:

- Tests T1 to T8 were dedicated to small granular systems (about 15 particles). The maximum compression force was set to 3 kN. For the monodisperse case (T1 to T6), the loading rate changed from one test to the next: ± 0.5 kN/s, ± 1 kN/s, ± 1.5 kN/s, ± 2 kN/s, ± 2.5 kN/s and ± 5 kN/s respectively. The objective here is to discuss the

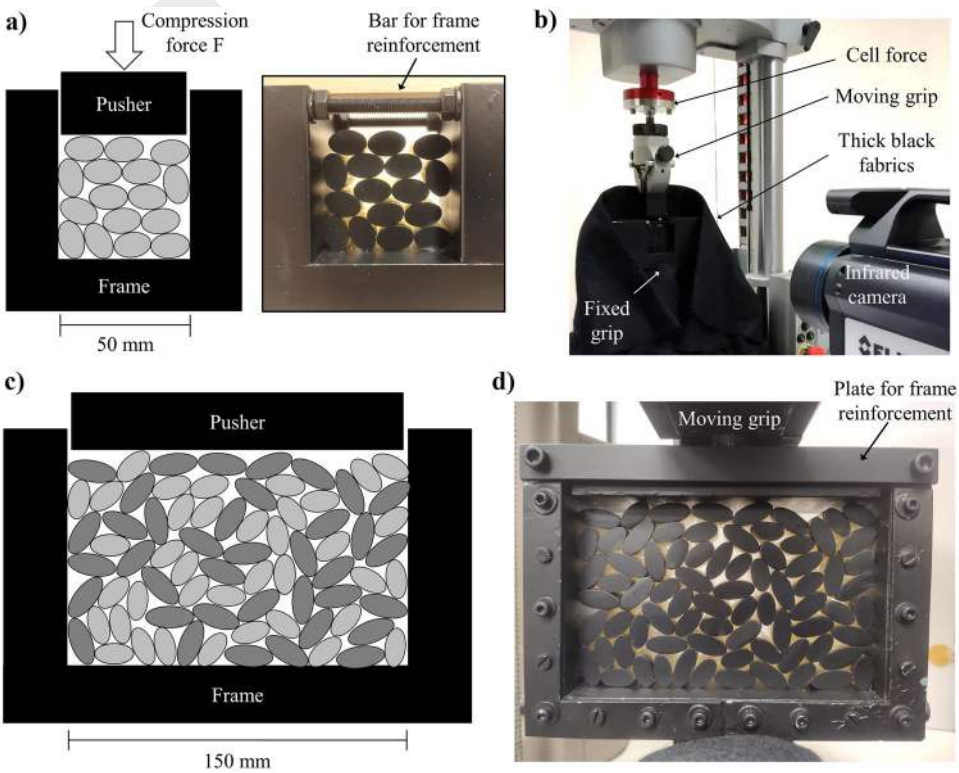

Fig. 2 Experimental setup: (**a**), (**b**) using a small frame for tests T1 to T8; (**c**), (**d**) using a larger frame for tests T9 to T11

Table 1 List and details of the tests presented in the paper

Test #	Type of granular material	Particle number	Content of the granular material	Maximum force	Force rate	Cycle duration	Number of cycles
T1	Monodisperse	16	16 small	3 kN	±0.5 kN/s	12 s	20
T2					±1 kN/s	6 s	
T3					±1.5 kN/s	4 s	
T4					±2 kN/s	3 s	
T5*					±2.5 kN/s	2.4 s	
T6					±5 kN/s	1.2 s	
T7*	Bidisperse	14	7 small + 7 large	3 kN	±2.5 kN/s	2.4 s	20
T8					±5 kN/s	1.2 s	
T9	Tridisperse	93	32 small + 31 medium + 30 large	6 kN	±1 kN/s	12 s	5
T10				9 kN		18 s	
T11				12 kN		24 s	

The asterisk symbol * indicates that the test was repeated with different spatial resolutions for the temperature fields (obtained in practice by using different optical conditions for the infrared camera)

influence of the loading rate in terms of viscosity and heat diffusion time (since, by construction, the shorter the mechanical cycle, the more adiabatic the thermodynamical response over the cycle). For the bidisperse case (T7 and T8), two loading rates were applied (±2 kN/s and ±5 kN/s respectively), the objective being to compare the results obtained with those of the monodisperse case.

- Tests T9 to T11 were devoted to a large granular system, with nearly 100 particles. The loading rate was fixed at ±1 kN/s for the three tests, but the maximum force was set to 6 kN, 9 kN and 12 kN respectively. The objective here is to discuss the influence of the applied load level. The influence of the loading rate was not studied here because this issue is discussed for the small monodisperse system. Note that the level of adiabaticity achieved during a test is expected to depend primarily on its duration, and not on the number of particles. This can be explained by their low thermal conductivity. Note also that keeping the same loading rate allows the same viscous behavior to be obtained for the three tests.

It should be noted that five preliminary mechanical cycles were applied to compact the granular systems (see Fig. 3(a)). Afterwards, the minimum force (10% of the maximum force) was held constant for about 10 min to ensure that the granular system had returned to thermal equilibrium with the environment before the beginning of the cyclic mechanical loading to be considered for the analysis. It can be noted in Table 1 that 20 cycles were applied to the small granular materials (T1 to T8) whereas only 5 cycles were applied to the large one (T9 to T11). This is because the high force levels applied in the latter case make the mechanical cycle long. To limit heat exchanges between the large granular system and its environment during the measurements, the number of cycles was limited to 5.

Two IR cameras featuring a similar Noise Equivalent Thermal Difference of 20 mK around ambient temperature were used to capture the temperature fields at the surface of the particles: a FLIR X6540sc camera (640×512 pixels) and a Cedip Jade III-MWIR camera (320×240 pixels). The former camera was used to study small granular systems in order to better understand the thermal response by "zooming in" on a few particles. The latter camera was used to study the large granular system in order to perform a macroscopic (*i.e.* statistical) analysis. The acquisition frequency was set to 10 Hz in both cases. Note however that with the Cedip camera, the base acquisition frequency was 100 Hz with a real-time averaging operation every 10 thermal images (leading to a recording frequency of 10 Hz), which enabled us to improve the thermal measurement resolution. Different spatial resolutions were considered during the test campaign. It is worth recalling here that granular materials under mechanical loading were subjected to stress concentrations at the interparticle contacts, thus leading by construction to differences in the full-field measurements as a function of the spatial resolution used. The spatial resolution value, defined here as the size of the IR pixel projected onto the measurement plane, is provided for each temperature map displayed below. Some tests were duplicated with different spatial resolutions (in practice by varying the distance between the camera and the granular material): mechanical conditions T5 and T7 were both performed twice, by using in each case a different spatial resolution. Note finally that the mechanical and thermal measurements were not synchronized in the experimental setup. The visualization of the displacements of the actuator in the temperature maps enabled us to distinguish between loading and unloading phases, but the resolution is not sufficient to identify phase maps.

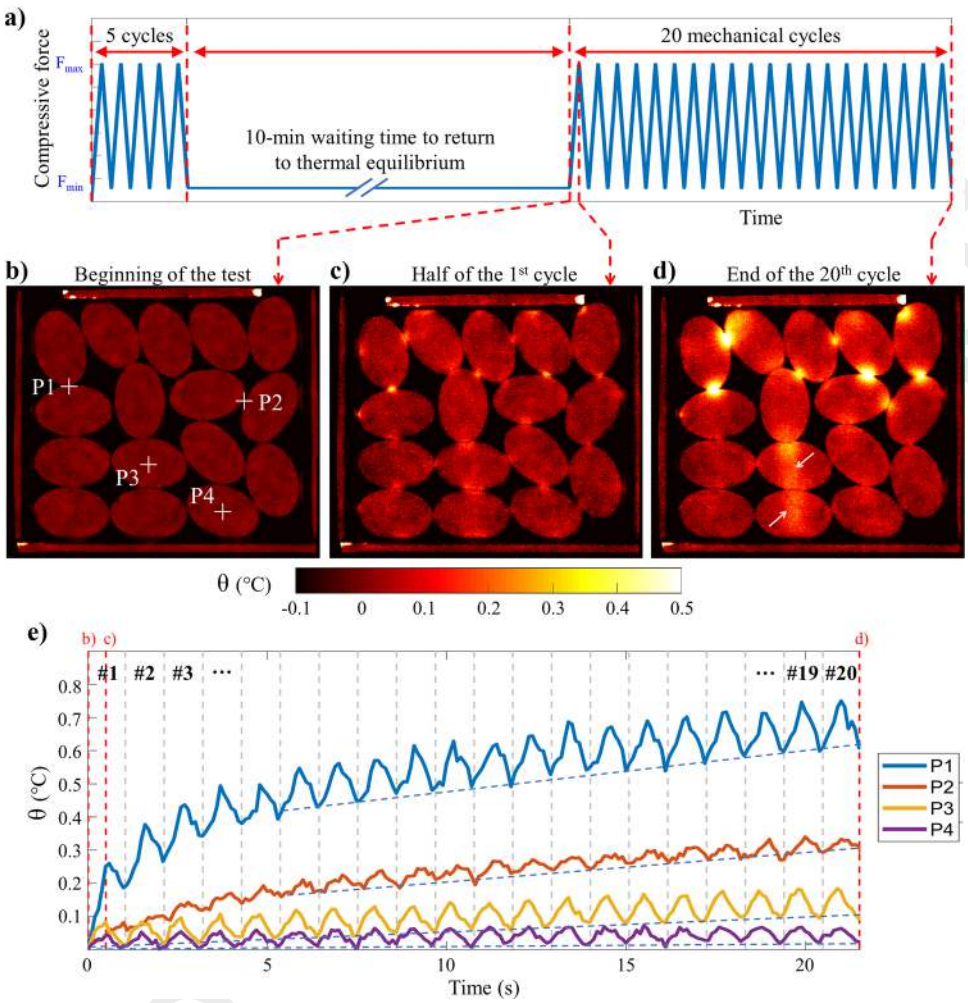

Fig. 3 (**a**) Schematic representation of mechanical loading; (**b**)–(**d**) maps of temperature changes during test T6 (monodisperse configuration, force rate ± 5 kN/s, maximum 3 kN). The spatial resolution of the thermal maps is equal to 131.6 µm; (**e**) temperature change as a function of time at four points in the granular material, after averaging over 9 × 9 px^2 (1.18 × 1.18 mm^2)

Finally, for each test, a reference thermal image was captured just before starting the cyclic mechanical loading, in order to identify the temperature *changes*. This quantity is denoted θ in the following. Note that despite the fact that TPU was in the rubbery state, particle deformations were actually "small" due to the limited magnitude of the external loading, as well as the confined nature of the compression. Before presenting the results of all the tests, the next section provides some preliminary observations concerning one of them in order to highlight the key points of the study.

Preliminary Observations

Before comparing the results of the tests described in Table 1, Fig. 3 shows a typical thermal response during a mechanical test, here test T6 (small granular system, monodisperse configuration, force rate ± 5 kN/s, maximum force 3 kN), with a spatial resolution of 131.6 µm for the temperature maps. The profile of the mechanical loading is recalled in Fig. 3(a). Several comments can be made about the thermal response:

- Figure 3(b)–(d) show the thermal fields at three times during the loading: beginning, half of the 1st cycle and end of the 20th cycle, respectively. Figure 3(c) highlights "hot" spots at nearly all the contacts. Figure 3(d) shows larger temperature changes at some interparticle contacts (especially in the upper part of the granular material) as well as a "hot" path through two particles (see white arrows).
- Four points of interest are selected in Fig. 3(b) to illustrate typical thermal responses *vs.* time. The choice of these points was made to open the discussion on the distinction between the effect of thermoelastic coupling (amplitude of thermal oscillation) and the effect of mechanical dissipation (overall self-heating tendency). Points P1 and P2 are located at interparticle contacts, while P3 and P4 are at the center of particles. Figure 3(e) presents the thermal variation $\theta(t)$ *vs.* time t for these four material points. Oscillation at the same frequency as the loading is observed. Loading is

accompanied by a temperature increase, whereas unloading is accompanied by a temperature decrease. Furthermore, a global increase is observed for the four points. A linear trend is obtained after the fifth cycle for points P1 and P2: see dashed lines. A self-heating rate of about 0.01 °C/cycle is measured at point P1 in the steady-state regime (from cycle #5). For P3 and P4, linearity is observed from the beginning of the test. It can also be noted that these four points exhibit distinct thermal responses in terms of *oscillation amplitude* (which can be a priori associated with the stress oscillation amplitude) and *average rate of increase* (which may be associated with mechanical irreversibility, such as damage, viscosity and friction). It is interesting to note that these two quantities are not always correlated. For example, point P2 is associated with a small oscillation amplitude and a high mean rate of increase, in contrast to point P3. The distinction between the calorific responses associated with thermoelastic behavior and anelastic behavior is the focus of the discussion proposed in the following sections.

- The thermal variation at point P4 shows an interesting property: a cyclic oscillation with nearly no overall increase, and a minimum value of θ remaining close to zero over the 20 cycles. It can be assumed that the response is here adiabatic and nearly reversible (we can guess that the strain and strain rate levels are low enough not to create much heat by viscosity or damage). Indeed, in this situation the amount of heat produced and absorbed (during loading and unloading respectively) by thermoelasticity is the same over a thermodynamical cycle. Thus θ returns then to nearly zero at the end of each cycle if the latter is adiabatic.

Some thermomechanical properties have been presented here to anticipate the discussion in the next sections. Before analyzing the results of the tests listed in Table 1, the next section provides the thermomechanics of materials background used for the analysis. It also presents the approach used for calorific data extraction.

Data Processing

Thermomechanics of Materials Background

The calorific response of materials subjected to mechanical loading can be split into two parts [39, 40]:

- The first part is associated with reversible thermomechanical phenomena, *i.e.* thermoelasticity only in most cases. As mentioned above in the introduction, two types of *thermoelastic coupling* (TEC) exist: one is governed by the change in internal energy (energetic elasticity) and the other is governed by the change in entropy (entropic elasticity) [34]. A simple uniaxial tensile test enables us to distinguish between them: upon loading (resp. unloading), energetic elasticity leads to a temperature decrease (resp. increase) whereas entropic elasticity leads to a temperature increase (resp. decrease). Actually, as both types of coupling exist in rubbery materials, a so-called *thermoelastic inversion* is observed upon loading, when the entropic contribution becomes preponderant [37]. On the contrary, uniaxial compression loading (resp. unloading) leads to a temperature increase (resp. decrease) for both types of TEC.
- The second part is associated with irreversible mechanical phenomena, which can be of different origins since they depend on the material and the loading conditions. The associated heat power density is called *mechanical dissipation* (MD) or *intrinsic dissipation*. This calorific quantity is always positive. It is for instance at the origin of the so-called *self-heating* of the material during cyclic loading due to fatigue damage and/or viscosity.

Figure 4 schematically illustrates the thermal variation in a rubbery material subjected to uniaxial compression cycles assuming an adiabatic evolution. Figure 4(a) corresponds

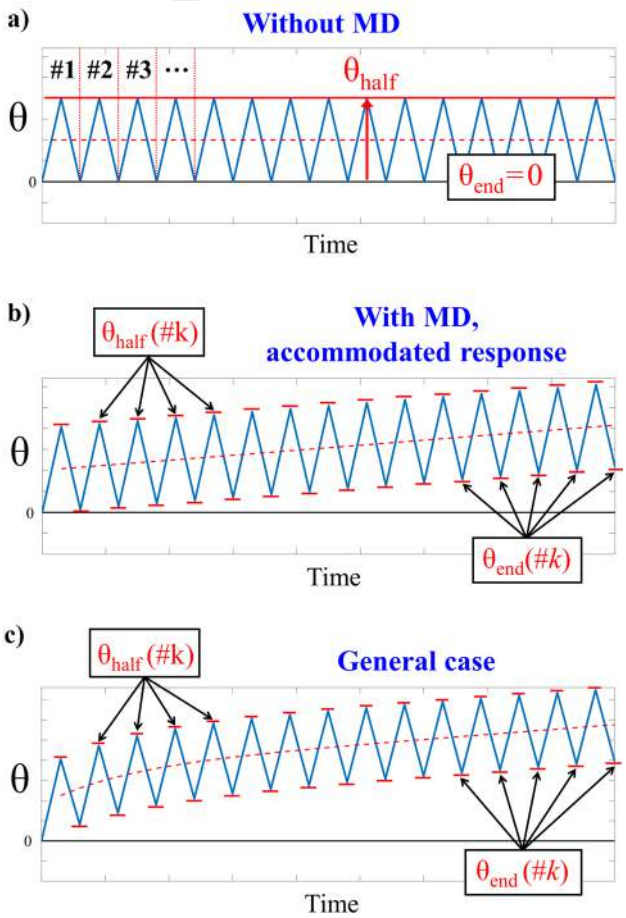

Fig. 4 Schematic temperature variations reflecting the contributions of thermoelastic coupling (TEC) and mechanical dissipation (MD) assuming adiabatic conditions in cyclic uniaxial compression

to the case of a purely thermoelastic response, *i.e.* without MD. The temperature change θ oscillates in phase with the mechanical loading between zero and a maximum value designated by θ_{half} in the following. The return to zero at the end of each cycle is due to the fact that the heat released during loading is equal in magnitude to that absorbed during unloading. Figure 4(b) corresponds to a case involving MD, assuming that the mechanical response of the rubbery matter is "accommodated" (stabilized mechanical response): the global temperature increase is linear considering that the same amount of MD is produced at each cycle. Figure 4(c) corresponds to a general case for which material accommodation occurs during the first cycles. Finally, we can recall that adiabaticity ("short" tests) is assumed in the temperature variations shown in Fig. 4. After a certain time, the red dashed lines on the graphs obviously tend to stabilize horizontally because of the balance between the heat produced by the MD and the heat exchanged with the environment.

Although local stress states in a granular material subjected to confined compression are more complex than in the case of simple uniaxial compression, some similarities can be noted between the temperature variations observed in Figs. 3(e) and 4. The curves in Fig. 4(a) (reversible response) and -b (accommodated response) may correspond to the thermal changes at points P4 and P3 in Fig. 3(e), respectively. The curve in Fig. 4(c) (non-accommodated general case) may correspond to the thermal changes at points P1 and P2, although material accommodation in the granular system was expected to be minimized due to the preliminary compression cycles. Complex thermomechanical responses are involved in a soft granular system, in particular associated with viscosity, multiaxial stress state and friction.

For the further processing of thermal data in the rest of the paper, two parameters are pointed out:

- the temperature change $\theta_{\text{end}}(\#k)$ at the end of the k^{th} cycle;
- the temperature change $\theta_{\text{half}}(\#k)$ at the middle of the k^{th} cycle, when the force level is maximum.

The following section develops some practical aspects of the image processing and the conversion into calorific quantities associated with TEC and MD.

Extracting Calorific Data

The basic idea of the subsequent processing is that the heat associated with TEC is null over an entire number of cycles and that the change is adiabatic. From a calorific point of view, the magnitude of the MD can therefore be quantified by the heat density Q_{MD} (in J/m^3) over *each cycle* as follows:

$$Q_{\text{MD}}(\#k) = \rho C\left[\theta_{\text{end}}(\#k) - \theta_{\text{end}}(\#k-1)\right] \tag{1}$$

where ρ and C are the density and the specific heat of the material, respectively. By construction, the total heat produced by the material over each adiabatic loading phase is given by:

$$Q_{\text{half}}(\#k) = \rho C\left[\theta_{\text{half}}(\#k) - \theta_{\text{end}}(\#k-1)\right] \tag{2}$$

This quantity implies a contribution from both TEC and MD. We propose to identify that of TEC by the heat density Q_{TEC} (in J/m^3) over each *half* a cycle as follows:

$$Q_{\text{TEC}}(\#k) = Q_{\text{half}}(\#k) - \frac{1}{2}Q_{\text{MD}}(\#k) \tag{3}$$

By nature, mechanical dissipation is always a positive calorific quantity (whatever the loading "direction", *i.e.* loading or unloading). Equation (3) implicitly assumes that MD is produced equally during the loading and unloading phases of each cycle, leading to the ratio of $^1/_2$ applied to the quantity $Q_{\text{MD}}(\#k)$ for the calculation of $Q_{\text{TEC}}(\#k)$. This hypothesis is strong, but remains reasonable as a first approach. Making a distinction between loading and unloading would be a relevant approach to be adopted in the future, in a way similar to the developments proposed in Ref [37] which deal with a rubbery (non-granular) material in uniaxial tension.

Remark 1 Because of the motion of the particles, it is tricky to deduce maps of $Q_{\text{half}}(\#k)$ and $Q_{\text{TEC}}(\#k)$. Indeed, particle locations are different at the lower and higher force levels. Since the particles slightly deformed, rigid-body movements were considered for the processing in the present study. Coupling IR thermography with measurements of displacement/strain fields by DIC in the visible range is a perspective of the present work to completely overcome this hurdle in a precise manner. The situation is simpler for the MD effect. Indeed, as the granular materials were previously compacted (see Fig. 3(a)), the particles returned to their positions at the end of each cycle, making it easy to obtain maps of $\theta_{\text{end}}(\#k)$ and $Q_{\text{MD}}(\#k)$ by simple image subtraction.

Remark 2 TEC is considered as a "strong" coupling in the sense that its magnitude is much higher than that of MD in most cases: $Q_{\text{MD}} \ll Q_{\text{TEC}}$. For instance, in the case of fatigue in steels, the ratio is of about three or four orders of magnitude [41]. For rubbers, the trend is the same, but MD may not be negligible due to viscosity or when the strain level increases: see Ref [37] dealing with uniaxial tensile tests of rubbers. This situation may make the measurement resolution of $Q_{\text{MD}}(\#k)$ disadvantageous compared to that of $Q_{\text{TEC}}(\#k)$. In order to improve the measurement resolution of the heat associated with MD in a steady-state cyclic regime, we decided to calculate also the *mean* value over several

cycles, starting from the fifth one (*i.e.* when the global temperature increases linearly, see the red dashed lines in Fig. 3(e)). This quantity is denoted $Q_{MD}(stab)$ in the following.

Remark 3 No irreversible movement of the particles was observed during the measurements. The contacts were "stabilized" by the preliminary compaction cycles. The particles remained in the same position during the measurements, with mainly contact deformations leading to slight translations and rotations of the particles. Furthermore, variations in interparticle contact areas with the load were observed. This results from the soft character of TPU. It can be considered that the overall behavior of the granular materials under study was mainly determined by contact deformations.

Remark 4 Several comments can be made about the boundary conditions. At both ends of all cylinders, the mechanical state is by construction of "plane stress" type because they are free boundaries. Friction at the contacts with the four walls certainly affects the stress state in the volume of the cylinders. Reducing the length of the cylinders would enable us to approach a plane state of stress in the volume, but this would lead to problems of stability in compression, and thus to safety issues during the tests. Limiting edge effects in a Schneebeli material can be achieved by increasing the number of cylinders. Another possibility is to use flexible boundaries, as in Ref [9]. See the perspectives of the present study in the "Conclusion" section.

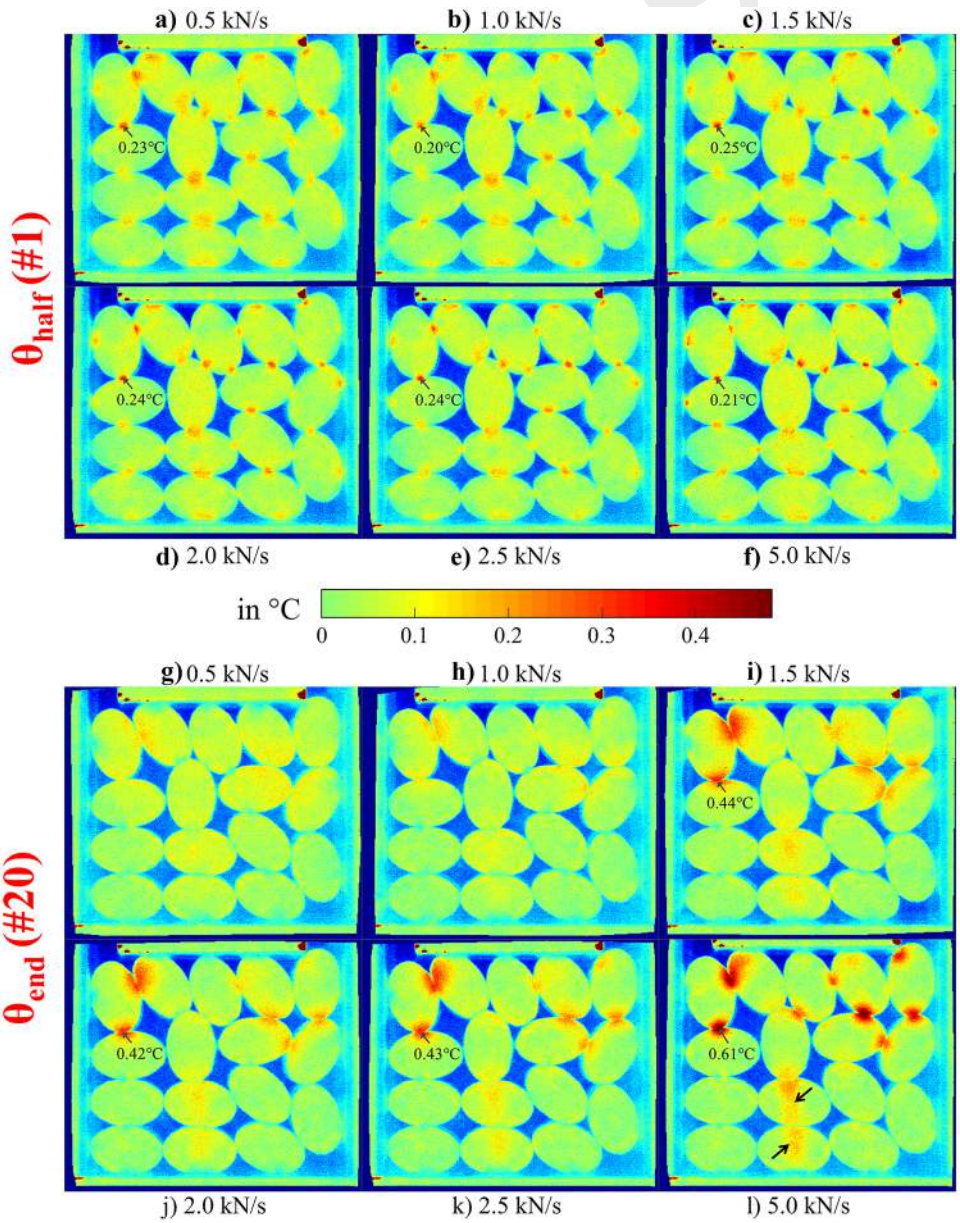

Fig. 5 θ_{half}(#1) and θ_{end}(#20) are the temperature changes in the middle of the 1st cycle and at the end of the 20th cycle, respectively. The spatial resolution of the maps is equal to 131.6 µm. Maximum values (after an averaging operation of 9×9 px^2) are also indicated

The next section proposes an application of the methodology to small granular materials by considering various aspects, in particular the influence of the loading rate and the spatial resolution of the thermal maps.

Application to Small Granular Systems

This section presents the results obtained for the "small" granular materials (16 particles in monodisperse configuration for tests T1 to T6; 14 particles in bidisperse configuration for tests T7 and T8) before applying the methodology to a larger system. The first part is dedicated to the analysis of the *thermal* responses (θ), in order to examine different aspects: influence of the loading rate; difference between the monodisperse and bidisperse systems; additional information on the influence of the spatial resolution used to measure the temperature fields. The analysis of the *calorific* response (Q_{TEC} and Q_{MD}) for a given test, namely test T6, is finally presented, before applying our approach to a more realistic granular system with more particles at the end of the paper.

Influence of Loading Rate

Figure 5 shows the influence of the loading rate on the small monodisperse granular system for the same maximum force, equal to 3 kN (tests T1 to T6). The spatial resolution of the thermal maps is equal to 131.6 µm. The following comments can be made concerning these maps:

- Figure 5(a)–(f) show the maps of θ_{half} (see Fig. 4(b), (c)) in the middle of the 1st cycle for a loading rate of ± 0.5 kN/s, ± 1 kN/s, ± 1.5 kN/s, ± 2 kN/s, ± 2.5 kN/s and ± 5 kN/s respectively. Temperature concentrations are visible at nearly all the contacts, including those with the metallic frame. The presence of these "hot" spots at the contacts can be related to stress concentrations, leading to stronger TEC and MD in these zones. Local temperature changes of up to 0.45 °C are measured (0.25 °C after averaging over 9×9 px^2, *i.e.*, 1.18×1.18 mm^2). The sizes of the hot spots are relatively similar between the tests. Thus it can be considered that the variation is adiabatic over a half-cycle in all the cases considered here. Close observation shows that these hot spots are actually slightly more concentrated when the loading rate increases. This can be explained by an increasingly adiabatic behavior when the period of the cycle decreases. Furthermore, there is no real difference in the intensity of these hot spots as a function of loading rate. Several decades of loading rate would probably be required to observe an increase in MD associated with viscosity.
- Figure 5(g)–(l) show the maps of θ_{end} measured at the end of the 20th cycle. Hot zones are visible at specific contacts in the upper part of the granular system, as well as inside two particles at the bottom part (see black arrows). Assuming that the heat due to TEC vanishes over entire numbers of cycles, these hot zones are caused by the MD. Heat diffusion over the duration of the 20 cycles is also potentially involved. It is worth noting that the loading rate has an influence on material viscosity and on the level of adiabaticity of the test: the higher the loading rate, the higher the heat produced by viscocity, and the better the adiabaticity level over the number of mechanical cycles which are applied. Note also that several decades of loading rate are generally required to see a significant influence of viscosity on the mechanical response of TPU. At the lowest rates (± 0.5 kN/s and ± 1 kN/s), the fields of θ_{end}(#20) are of low intensity. They are also only slightly localized. This is a priori the consequence of the heat diffusion during the 240 s required to complete the 20 cycles. The rates of ± 0.5 kN/s and ± 1 kN/s can be considered as too small to consider the variation as adiabatic over the test duration. The maps of θ_{end}(#20) at ± 1.5 kN/s, ± 2 kN/s and ± 2.5 kN/s are quite similar, with concentrations of same sizes and same intensities. The maximum value is about 0.43 °C for these three tests. It can be considered that these three tests are adiabatic, with similar viscosity effects. The test at the highest loading rate (± 5 kN/s) presents the strongest thermal response, with a maximum value of 0.61 °C. In addition, material self-heating is clearly evidenced along the hot path which is visible through the two particles in contact marked by black arrows. This is a clear effect of the increase in viscosity with the loading rate.

In the following, heat is calculated for test T6 (at ± 5 kN/s), as it presents the highest level of adiabaticity over the duration of the 20 mechanical cycle tests.

The orders of magnitude of the maximum values of θ_{half}(#1) and θ_{end}(#20) appear to be similar. However, it must be recalled that the values were measured at the first half cycle and the end of the 20th cycle respectively. A "calorific" comparison between the two heat sources (TEC and MD) within one cycle will be presented later.

Comparison Between Monodisperse and Bidisperse Systems

Figure 6 presents a comparison between a monodisperse configuration (test T6) and a bidisperse configuration (test T8) for the same loading conditions (loading rate = ± 5 kN/s, maximum force = 3 kN). The spatial resolution of the maps is again equal to 131.6 µm. It is confirmed in the bidisperse case that concentrations of θ_{half}(#1) occur at each contact, whereas concentrations of θ_{end}(#20) only exist at some contacts and within certain particles. The thermal response

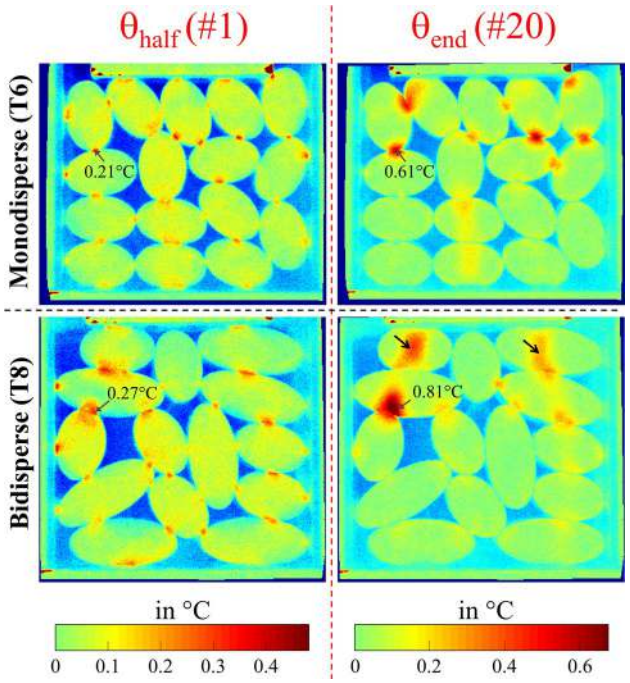

Fig. 6 Comparison between monodisperse configuration (test T6) and bidisperse configuration (test T8) with same loading conditions (force rate ± 5 kN/s, maximum 3 kN). The spatial resolution of the thermal maps is equal to 131.6 µm. In each map, the maximum value (after an averaging operation of 9×9 px^2) is indicated

appears to be stronger in the bidisperse system than in the monodisperse one. The maximum value of θ_{half}(#1) is higher in the former case: 0.27 °C *vs.* 0.21 °C after averaging over 9×9 px^2, *i.e.*, 1.18×1.18 mm^2. The same conclusion holds for the maximum value of θ_{end}(#20): 0.81 °C *vs.* 0.61 °C. Since the void ratio is higher in the bidisperse system (it is less compact than the monodisperse one), the stress level in the particles is also expected to be higher. This explains a stronger thermal signature for the mechanical response in the bidisperse system. Note also that the hot zones are more widely spread in the bidisperse case. Logically, the higher the magnitude of the interparticle force, the larger the contact area: see for instance the temperature distribution around the 0.27 °C location in the θ_{half}(#1) map. In the θ_{end}(#20) map for the bidisperse system, hot paths are visible in the two particles in contact with the pusher (see black arrows). The high load levels in these two particles can be explained by the fact that the vertical force is transmitted by only 2 contacts with the pusher in the bidisperse configuration *vs.* 4 contacts in the monodisperse configuration (see the θ_{half}(#1) maps showing the "active" contacts). Two tests are not sufficient to draw general conclusions at the local scale, as the response strongly depends on the location and orientation of the particles with respect to each other. However, the comparisons made here seem logical.

Improved Spatial Resolution

Figure 7(a), (b) show thermal maps for the monodisperse and bidisperse configurations respectively, and for the same loading conditions (loading rate = 2.5 kN/s, maximum force = 3 kN, tests T5 and T7 respectively), but the spatial resolution is different from that used in the previous figures. The spatial resolutions were equal to 41.0 µm and 66.3 µm, respectively, thus enabling us to zoom in on small zones in the granular systems. The locations of the enlarged zones Z1 and Z2 are indicated in the schematic views. For zone Z1, a comparison

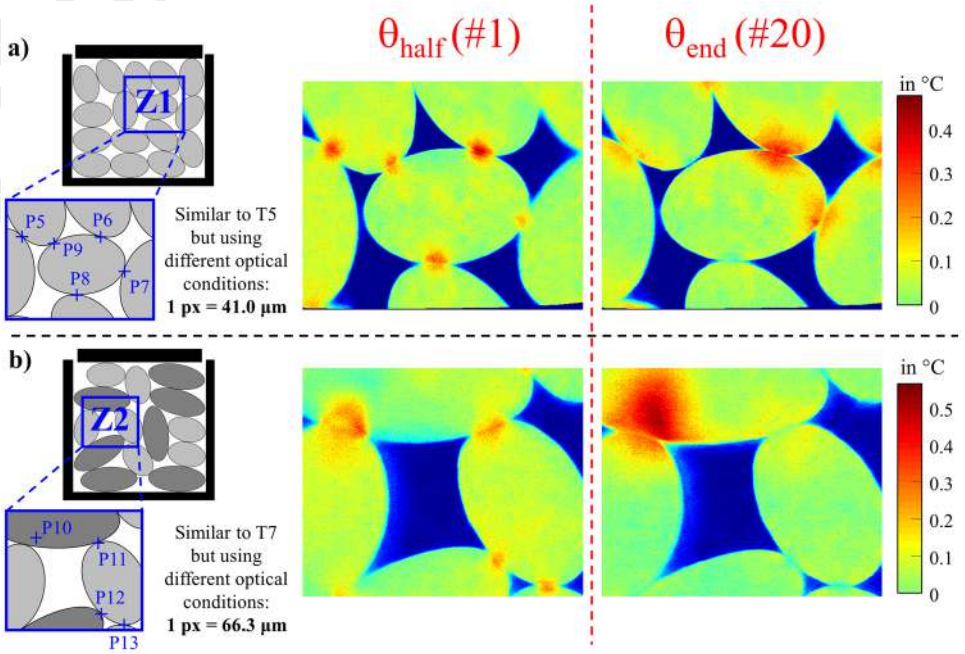

Fig. 7 Comparison between monodisperse and bidisperse configurations with the same loading conditions (force rate ± 2.5 kN/s, maximum 3 kN) but using smaller spatial resolution compared to tests T5 and T7, respectively. See Table 2 and Fig. 8 for comparison with measurements at 131.6 µm spatial resolution

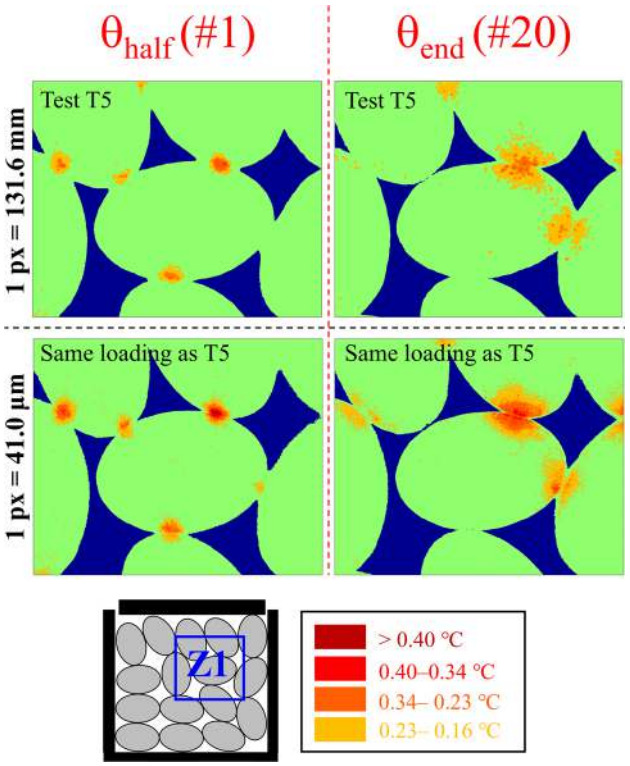

Fig. 8 Comparison of results depending on the spatial resolution in zone Z1 for two similar tests (monodisperse configuration, force rate ± 2.5 kN/s, maximum 3 kN, minimum 0.3 kN)

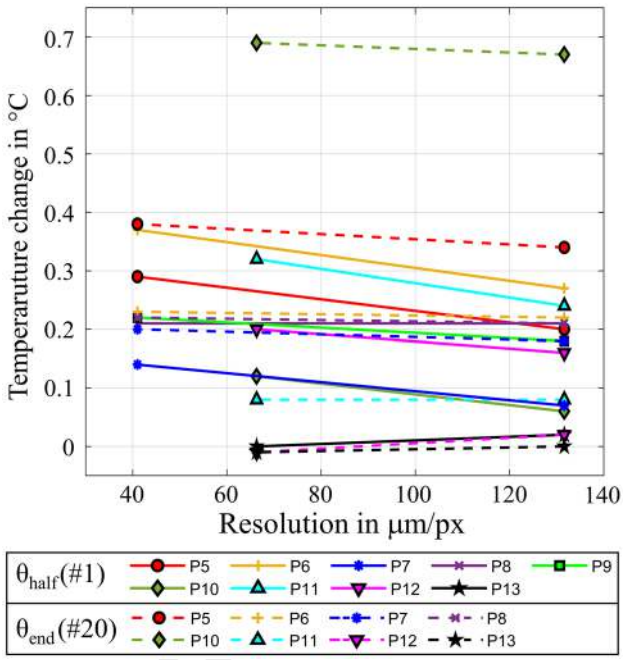

Fig. 9 Temperature changes at various points in the two small granular systems (see locations in Fig. 7) as a function of a pixel size projected on the measurement surface, and for the same loading conditions (force rate ± 2.5 kN/s, maximum 3 kN, minimum 0.3 kN)

with previous maps at 131.6 µm is also presented in Fig. 8 by using five color yields. It can be seen that the distributions are globally the same for both maps θ_{half}(#1) and θ_{end}(#20), whatever the spatial resolution. The same conclusion was obtained for zone Z2 (color yield images not presented here). Some points of interest are indicated in Fig. 7 for comparison purposes: P5 to P9 in zone Z1; P10 to P13 in zone Z2. It can be seen that the maximum contact temperatures are not exactly located at the boundary between the particles (see in particular P10). In practice, the values of θ_{half}(#1) and θ_{end}(#20) that are reported in Table 2 are the maximum ones in the contact zones. It can be seen that certain extracted maximum values significantly depend on the spatial resolution used. The graph in Fig. 9 shows the variation of the extracted values as a function of the pixel size projected on the measurement surface. It can be seen that, except for the smallest values (no temperature concentration), the better (*i.e.* the lower) the spatial resolution, the higher the maximum temperature which is measured. This situation is inherent to the use of a full-field measurement technique in the

Table 2 Comparison of results depending on the spatial resolution for the same loading conditions (force rate ± 2.5 kN/s, maximum 3 kN, minimum 0.3 kN). Note that the maximum temperature corresponding to P10 is not located at the boundary between the particles

Zone	Point	Test T5 for Z1 and test T7 for Z2 (1 px = 131.6 µm)		Same loading conditions with another spatial resolution (41.0 µm for Z1 and 66.3 µm for Z2)	
		θ_{half} (#1) in °C	θ_{end} (#20) in °C	θ_{half} (#1) in °C	θ_{end} (#20) in °C
Z1	P5	0.20	0.06	0.29	0.12
	P6	0.27	0.24	0.37	0.32
	P7	0.07	0.16	0.14	0.20
	P8	0.21	0.02	0.21	0.00
	P9	0.18	No contact	0.22	No contact
Z2	P10	0.34	0.67	0.38	0.69
	P11	0.22	0.08	0.23	0.08
	P12	0.18	0.02	0.20	-0.01
	P13	0.21	0.00	0.22	-0.01

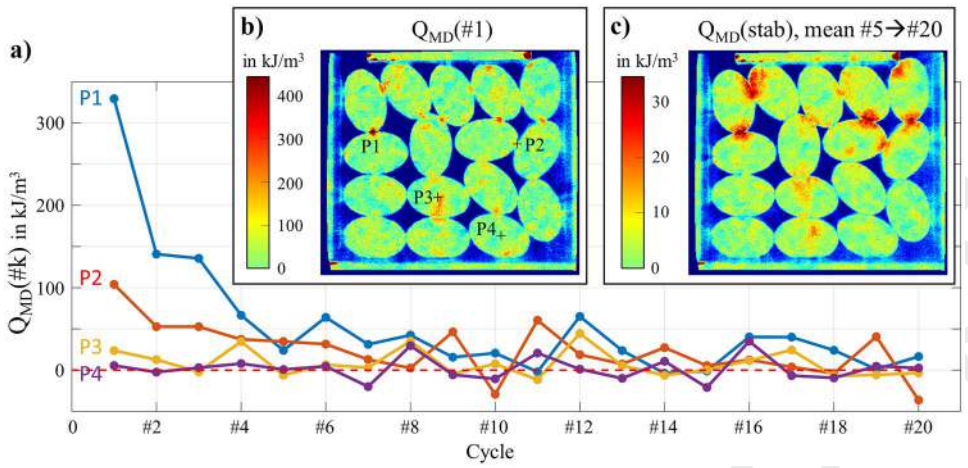

Fig. 10 Heat produced by mechanical dissipation (MD) during each mechanical cycle during test T6 (monodisperse configuration, force rate ± 5 kN/s, maximum 3 kN): (**a**) variations along the cycles at four points after an averaging operation of 9×9 px^2; (**b**) over the first cycle; (**c**) average over the fifth to twentieth cycles. The spatial resolution of the maps is equal to 131.6 µm

case of localized phenomena. This could be a problem for the estimation of gradients (for estimating heat diffusion). By nature, localizations take place in granular materials, thus making a calorific analysis of this type of material difficult to perform in non-adiabatic conditions. In any case, for a thermomechanical analysis, any comparison between different maps should be made using the same spatial resolution.

Calorific Analysis

The objective here is to validate the data processing providing calorific data for one test, namely T6 (monodisperse configuration, force rate ± 5 kN/s, maximum 3 kN). In particular, it is a question of comparing the heat produced by the mechanical dissipation $Q_{MD}(\#k)$ at each cycle (see Equation (1)) and the heat produced by the thermoelastic coupling at each half-cycle $Q_{TEC}(\#k)$ (see Equation (3)):

Figure 10(a) shows the variation in $Q_{MD}(\#k)$ at four points in the granular system. It can be seen that the values for points P1 and P2 rapidly decrease along the first five cycles. The maximum values measured for the first cycle (more than 300 kJ/m^3) appear to be more than half those of Q_{TEC} (more than 600 kJ/m^3); compare the map of Q_{MD}(#1) in Fig. 10(b) with the map of Q_{TEC}(#1) in Fig. 11(a). Thus, MD plays an important role in the temperature variations during the first five cycles. This result can be explained by a continuation of material accommodation during the five first cycles, as already discussed from the temperature variations. From the fifth cycle on, the value of $Q_{MD}(\#k)$ at the four points seems to fluctuate around zero. However, they are positive on average: see Fig. 10(b) showing the maps of Q_{MD}(stab), which is the average of $Q_{MD}(\#k)$ over cycles #5 to #20. Maximum values reach about 30 kJ/m^3. These small values for Q_{MD}(stab) are also not negligible as they are at the origin of the global temperature increase represented by the dashed lines in Fig. 3(e). A final remark can be made about the maps of $Q_{TEC}(\#k)$. The value does not really change over the cycles: compare cycle #1 (Fig. 11(a)) and cycle #20 (Fig. 11(b)). This can be explained by a stabilized elastic

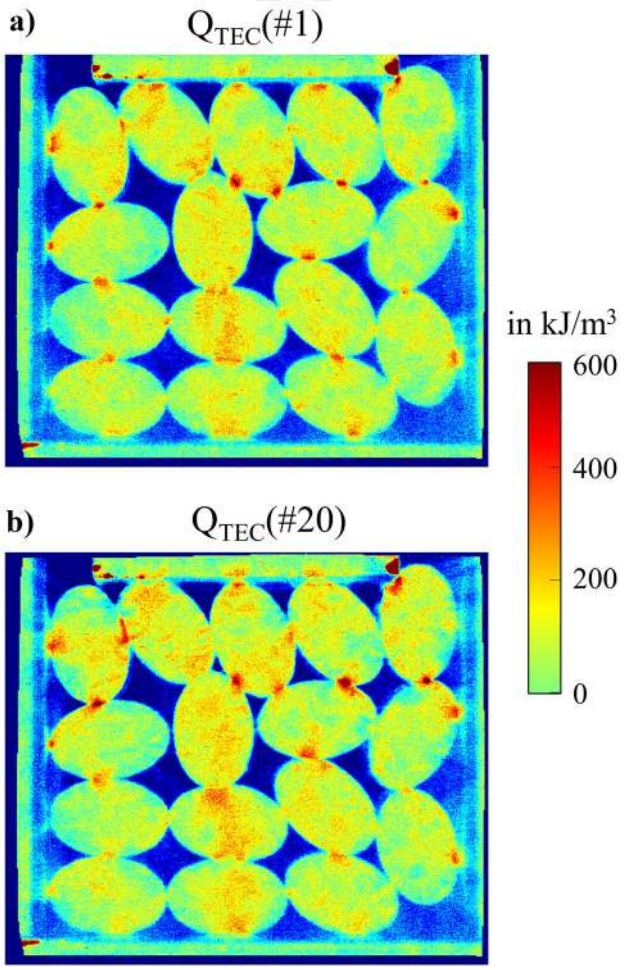

Fig. 11 Heat produced by thermoelastic coupling (TEC) over the loading phase during test T6 (monodisperse configuration, force rate ± 5 kN/s, maximum 3 kN): (**a**) in the first cycle; (**b**) in the twentieth cycle. The spatial resolution of the maps is equal to 131.6 µm

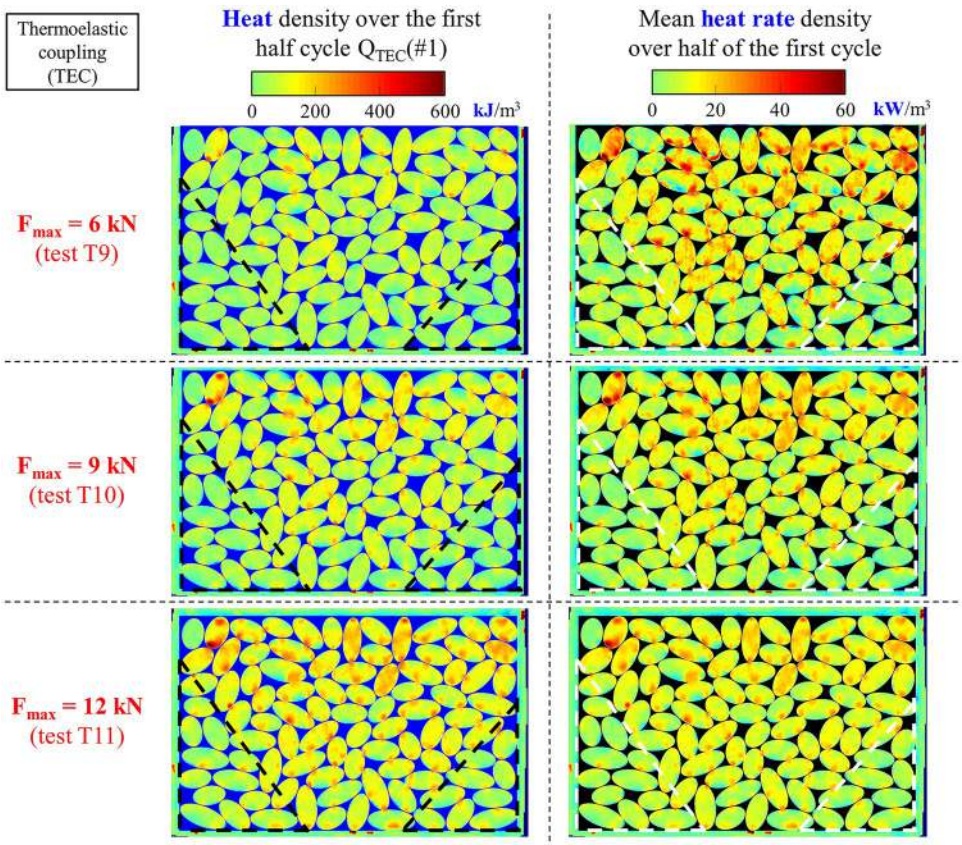

Fig. 12 Thermoelastic coupling in the tridisperse granular material during the first half cycle. Left column: heat density over half a cycle; right column: corresponding mean heat rate density

response due to the preliminary five cycles which compacted the granular material before performing the test. It can also be noted that high values are not only observed in the contact zones. Significant TEC is also revealed inside some particles. Finally, it is confirmed that TEC is a strong coupling in the steady-state cyclic regime. Indeed, the maximum values of Q_{TEC} exceed 600 kJ/m^3, whereas those of Q_{MD}(stab) only exceed 30 kJ/m^3.

Various observations were made here on small discrete systems. They show that is it possible to obtain thermal and calorific information based on the proposed methodology. The next section is dedicated to a more realistic granular material case, since it comprises nearly 100 particles, thus enabling us to perform a statistical analysis.

Thermomechanical Behavior of a Larger Granular System

This section presents an analysis of the thermomechanical response of the "large" tridisperse granular material made with about 30 particles of each type (see Table 1). The spatial resolution is now equal to 496 µm. The following three points are successively discussed:

- influence of the force level reached, namely 6 kN, 9 kN and 12 kN (tests T9, T10 and T11 respectively), at the same loading rate ± 1 kN/s;
- analysis of a potential correlation between calorific response and interparticle movements;

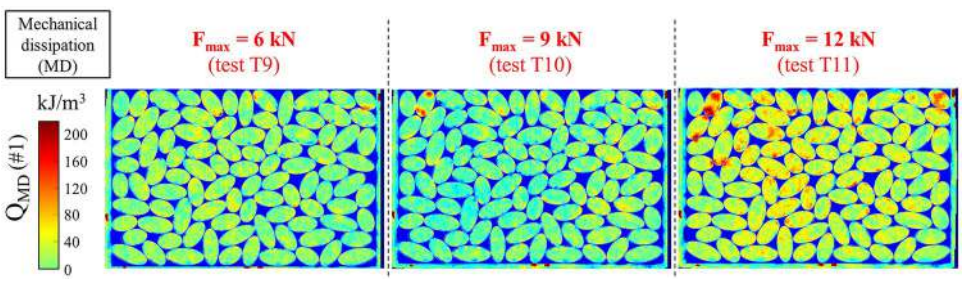

Fig. 13 Mechanical dissipation in the tridisperse granular material: heat density over the first cycle

- statistical analysis from the nearly 600 interparticle contacts in the granular system.

Influence of the Force Level Reached

Figure 12 shows maps related to the thermoelastic coupling contribution for the three tested loading levels during the first half cycle. Results are first displayed in terms of Q_{TEC}(#1) *heat* density: see the left-hand side of this figure. Logically, the higher the force level reached, the higher the values due to the increased stresses in the granular system. The results are also presented in terms of *mean heat rate* density, corresponding to the value of Q_{TEC}(#1) divided by the duration of half a cycle: see the right-hand side of the figure. It can be observed that these maps now in kW/m^3 are quite similar for the three loading levels. This result may appear surprising for a material featuring non-linear elasticity such as TPU. It can be explained by an operating loading range in the linear part of the TPU's mechanical response (low deformation of the particles during the test). Hot zones are observed at nearly all the interparticle contacts. It can be noted that the highest values are located at the upper left and right corners of the granular system. The lowest and least diffuse concentrations are in the bottom left- and right-hand zones of the granular system (see dashed triangular zones). This observation is quite similar to a previous result obtained on another type of granular material, namely a monodisperse system made of rigid particles, see Fig. 8 in Ref [32]. This phenomenon is a priori related to the boundary conditions. The number of particles is probably not sufficient to limit these boundary effects.

Figure 13 shows maps related to the mechanical dissipation contribution for the three loading levels that were tested. The results are displayed in terms of heat density over the first cycle Q_{MD}(#1). Note that the adiabaticity of the tests is questionable due to the long duration of the mechanical cycles (12 s, 18 s and 24 s for tests T9, T10 and T11 respectively, see Table 1). Moreover, maps of Q_{MD}(stab) cannot be calculated due to the number of mechanical cycles, limited to 5. In any case, some results can be extracted. As expected, the higher the force level, the higher the anelasticity level. The highest values are located at the upper left and right corners of the granular system. On the one hand, this is logical because high stress levels (revealed by strong TEC in Fig. 12) are expected to be also a priori associated with high mechanical irreversibility levels (strong MD). On the other hand, tangential interparticle forces may create high friction without necessarily creating high stress concentrations, which may partially explain the difference between the TEC and MD responses. The next section aims to propose a potential correlation between calorific response and interparticle movements.

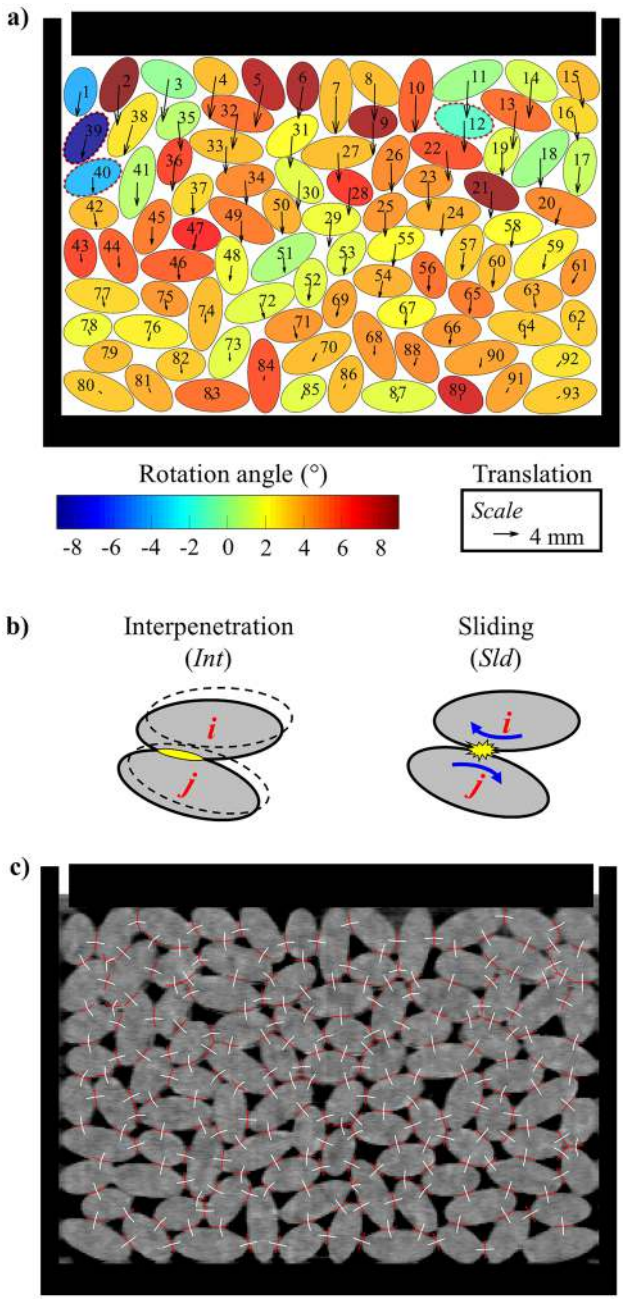

Fig. 14 Movement of the particles: (**a**) example for test T11; (**b**) illustration of interparticle movement indicators; (**c**) identification of normal (small white lines) and tangential (small red lines) directions at each contact

Interparticle Movements and Calorific Responses

For illustration purposes, the interparticle movements in the tridisperse granular system for the maximum force of 12 kN (test T11) are shown in Fig. 14(a), distinguishing between translation and rotation. It was necessary to measure these latter quantities in order to subsequently calculate relative

movement at all the contacts (see Appendix). The objective is then to compare kinematic quantities (whose calculation involves these translations and rotations) with calorific quantities (whose calculation involves temperature changes). The coordinates of the interparticle contacts and ellipse centers, as well as the orientation of the ellipses, were extracted at the minimum and maximum loads by hand, which is feasible for less than 100 particles. The translation field is displayed by arrows whose length is proportional to the magnitude of the translation of the particle center. As expected, the magnitude decreases from the pusher to the bottom of the fixed frame. In the lower part of the granular system, the directions are globally symmetrical with respect to the vertical median plane. The rigid-body rotation field is displayed by colors. It can be observed that the angles are mainly positive (trigonometric sense). Negative values are only observed in the upper part, especially near the top left corner. More importantly, interparticle motions deserve to be analyzed, as they are directly related to potential thermomechanical effects. This was performed via two interparticle movement indicators: *interpenetration* and *sliding*: see Fig. 14(b). The calculation of these two parameters requires the knowledge of the normal and tangential directions at each contact: see the small white and red lines, respectively, in Fig. 14(c). Their identification was performed by manually extracting geometric data directly from the thermal maps: inclination and location of the center of each ellipsoidal particle; location of each contact. In addition, the procedure was performed for both sides of each contact, which justifies the pair of normals (small white lines) and the pair of tangents (small red lines) displayed at each contact in the image. Slight differences are sometimes observed between the two sides, due to the difficulty in manually extracting geometric information with the low spatial resolution of an IR camera (compared to visible range cameras). An averaging operation was therefore performed between the two sides of each contact to determine one single normal direction and one single tangential direction each time. From the translation and rotation data, it is

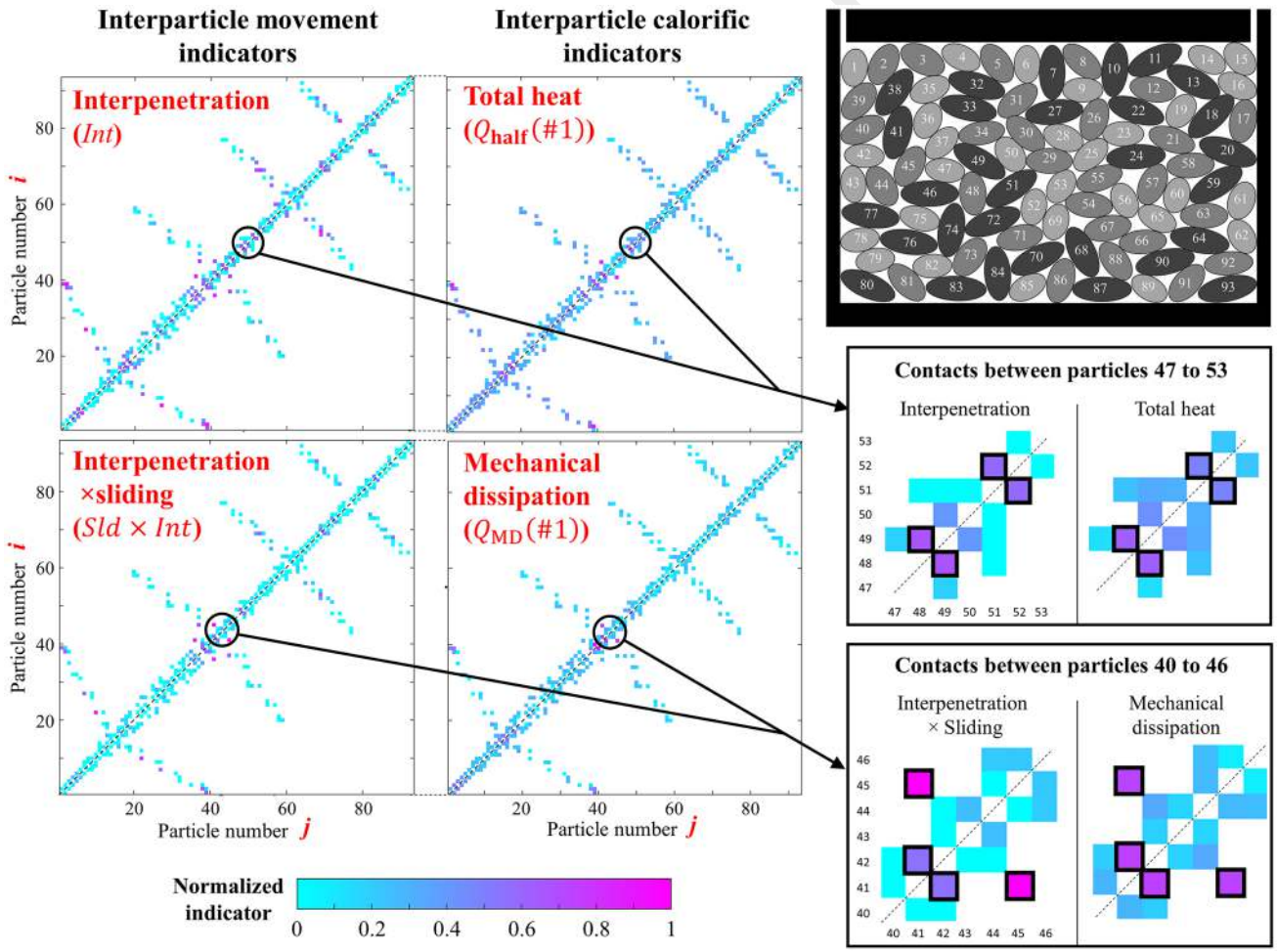

Fig. 15 Comparison between interparticle movement indicators and contact calorific indicators for test T11

then possible to calculate the interpenetration (*Int*) and the sliding (*Sld*) at each contact. Appendix describes the complete mathematical procedure used to calculate these values.

Figure 15 shows the distributions of *Int* and $Int \times Sld$, whose values have been normalized by dividing them by their respective maximum values. The distributions are presented through a matrix whose row i and column j correspond the numbers of the particles in contact (see these numbers in the schematic view in the upper right corner of the figure). The objective is to compare them with the values of $Q_{half}(\#1)$ and $Q_{MD}(\#1)$ respectively, at the contacts. Indeed, it is expected that the higher the interpenetration, the greater the heat produced by the material $Q_{half}(\#1)$, which involves both TEC and MD contributions. It is also expected that MD at the contacts is strongly related to friction, which is here "mechanically" expressed by the product $Int \times Sld$. Indeed, the contact normal force is proportional to the interpenetration *Int* in the case of a contact between two elastic cylinders (see equation 5.34 in Page 63 in Ref [42]). Moreover, the curvature radii do not appear at all in the relationship between force and interpenetration [42]. Assuming also that the tangential force is proportional to the normal force during sliding (Coulomb's law), the product $Int \times Sld$ is therefore representative of the mechanical work associated with friction. The calorific indicators $Q_{half}(\#1)$ and $Q_{MD}(\#1)$, were manually extracted at all couples of particle i and j in contact. It is worth noting that, due to the large spatial resolution (496 µm) compared to the measurements in the small granular materials in the previous sections, the extracted values are actually strongly averaged. Normalization of $Q_{half}(\#1)$ and $Q_{MD}(\#1)$ by their maximum values over all the contacts was also performed. It is certainly illusory to try to find a precise correlation between these mechanical (*Int* and $Int \times Sld$) and calorific ($Q_{half}(\#1)$ and $Q_{MD}(\#1)$) indicators. However, some agreements can be found at certain contacts: see for example the two insets in Fig. 15. The higher values are fairly well correlated: see black squares at contacts 48/49 and 51/52 for the comparison between *Int* and $Q_{half}(\#1)$, and at contacts 41/42 and 41/45 for the comparison between $Int \times Sld$ and $Q_{MD}(\#1)$. Various approaches can be proposed to improve results in the future, such as defining other mechanical indicators and using measurements of displacement/strain fields by DIC in the visible range. Nevertheless, a statistical analysis is presented in the next section concerning the TEC interparticle data. The analysis is not pursued for the MD interparticle data because most of them are low and affected by noise (the highest values are mainly located in the upper left and right corners of the granular material). Higher loading rates and averaging over multiple steady-state cycles could result in a better signal-to-noise ratio for the MD response in the future.

Statistical Analysis of the Thermoelastic Coupling Signature at the Interparticle Contacts

Figure 16(a) shows the distribution of the calorific signatures $Q_{TEC}(\#1)$ associated with TEC at the interparticle contacts in the tridisperse system for the maximum force, 12 kN. The mean value is also indicated (see vertical dashed line), as well as the corresponding probability density function (PDF) that was fitted using a generalized extreme value distribution. This type of function was chosen due to the asymmetric distribution between low and high values. The comparison between the three force levels tested (6 kN, 9 kN and 12

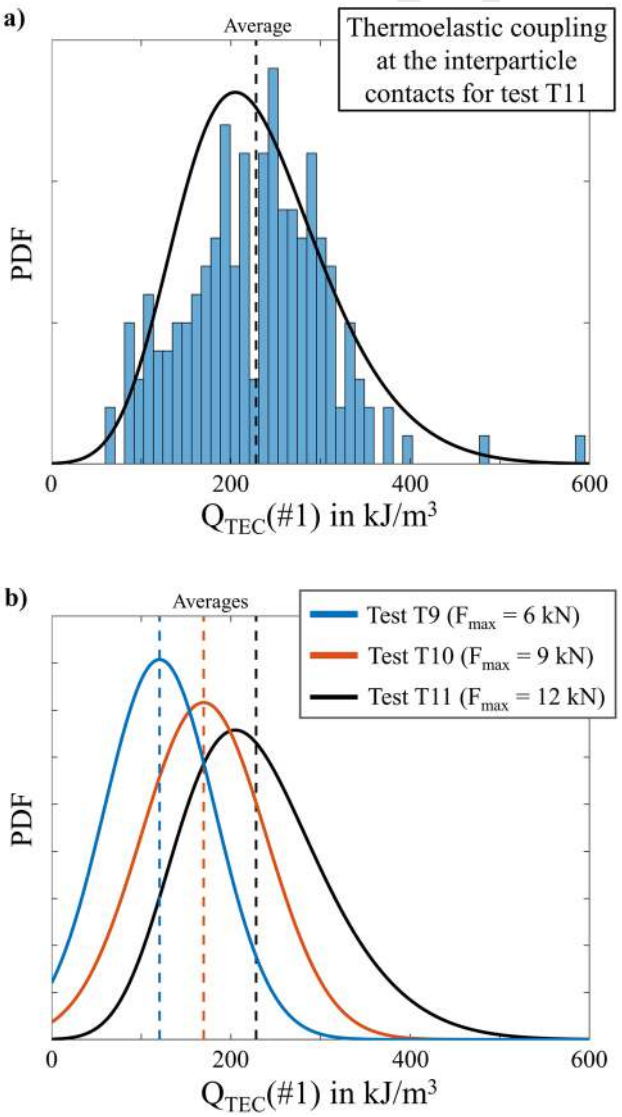

Fig. 16 Calorific signature associated with thermoelastic coupling at the interparticle contacts in the tridisperse system: (**a**) example of histogram and corresponding probability density function (PDF) using a generalized extreme value distribution; (**b**) comparison of the PDFs for the three loading levels

kN) is presented in Fig. 16(b). Logically, an increase in the average value is observed with the maximum force level. The PDFs are indeed shifted to the right in the graph and are wider when the maximum force increases. These results are quite logical, but show that IR thermography and subsequent calorific analysis provide interesting/complementary data for the analysis of the thermomechanical behavior of granular materials, as discussed in the "Conclusion" section.

Conclusion

For several decades, the analysis of the mechanical behavior of continuous solids has benefited from full-field measurement techniques using infrared thermography and subsequent calorimetry processing. Indeed, the experimental evidence of local couplings between mechanical and thermal responses has enabled a real analysis of heterogeneous phenomena in continuous materials within a rigorous thermodynamic framework. Until now, granular materials have been virtually excluded from this approach in the experimental mechanics community. We believe that such an experimental procedure can also provide information of interest for the understanding of the mechanical behavior of granular materials, which is potentially complementary to full-field strain measurements and numerical methods.

In the present study, soft granular systems composed of elastomeric particles were selected to take advantage of the thermoelastic coupling (TEC) associated with entropic elasticity. Centimeter-sized cylinders with ellipsoidal cross sections were elaborated to form the particles. The thermal response of monodisperse, bidisperse and tridisperse systems was measured by infrared camera under confined cyclic compression. A temperature oscillation featuring the same frequency as that of the load was observed. During the compression phases, hot spots were identified at all interparticle contacts. This was explained by the entropic TEC activated by stress concentrations at the contacts, with a potential contribution of mechanical dissipation (MD) associated with irreversible phenomena such as viscosity and friction. The importance of the spatial resolution used for the thermal measurements was highlighted. Local temperature changes of up to nearly 0.5 °C were measured at a spatial resolution of about 0.1 mm. The value is halved at a spatial resolution of about 1 mm. Self-heating over the cycles was also observed around specific contacts, as well as inside some particles. This is caused by MD, considering that the heat associated with TEC vanishes over a mechanical cycle. Self-heating rates up to about 0.01 °C/cycle were measured in the steady-state regime. A greater contribution of MD was observed during the first cycles. A comparison between monodisperse and bidisperse systems at the same macroscopic loading level showed a stronger thermal response in the former case, in agreement with the expected differences in the intensity of interparticle contact forces. Calorimetric treatment allowed us to calculate the corresponding heat values. It was estimated that the intensity of the heat generated by entropic TEC could reach more than 600 kJ/m^3 in the contact zones during the compression phases, while that associated with MD was limited to about 30 kJ/m^3/cycle in the steady-state regime (and about 300 kJ/m^3/cycle in the transient regime). This shows that TEC is a strong coupling. TEC data were processed for a tridisperse system consisting of about 600 interparticle contacts. Statistical information on the TEC heat distribution at the interparticle contacts shows a change in the distributions with the level of compression that is applied. This paves the way for thermomechanical models based on such calorimetric data. Several extensions of this work can be proposed:

- increasing the number of particles; the objective would be to provide statistical calorific data on both reversible and irreversible mechanical phenomena excluding boundary effects;
- coupling infrared thermography with visible-range measurements to measure the strain fields at the same time as the temperature maps; this should enable us to calculate energy balance;
- increasing the complexity of the shapes of the cylinder cross-sections, including for example sharp edges and non-convex geometries;
- modeling and simulating the thermomechanical experiments; this would require a coupling of discrete and finite element methods. The comparison between numerical and experimental methods for soft granular media is a further step of our work;
- proposing a macroscopic thermodynamical model; this approach would require appropriate averaging operations to obtain calorimetric data (TEC, MD) to be related to mean mechanical variables (fabric stress and/or strain). This could lead to the proposition of macroscopic/mesoscopic stress measurement techniques by using only temperature data;
- applying the proposed approach to sand; the design of the experimental device would however be an issue. Indeed, the box containing the sand should simultaneously sustain the stress induced by the load and be infrared transparent, so that the IR camera could observe and capture the temperature field over one of the walls during the tests. The application of the proposed thermodynamical methodology to sand would thefore require significant implementation efforts.

Appendix: Estimating Interpenetration and Sliding Between Cylinders with Ellipsoidal Cross Section

We consider two cylinders S_1 and S_2 in contact at point I, see the schematic view in Fig. 17. The objective here is to properly define how to estimate the relative movement at the contact between S_1 and S_2. Assuming that the movement in terms of rotation and translation is small, the rigid-body movement of each cylinder S_i, $i = 1, 2$ can be modeled by two vectors $\underline{\Theta}_i$ and $\underline{U}_{O_i}$ where O_i is the center of each cylinder S_i. Vectors $\underline{\Theta}_i$ and $\underline{U}_{O_i}$ are respectively the rotation vector of S_i and the displacement vector of its center O_i. The coordinates of all the points represented in the figure are assumed to be identified manually in the images of the deformed and current configurations taken by the IR camera during the test. The components of vectors $\underline{U}_{O_1}$, $\underline{U}_{O_2}$, $\underline{\Theta}_1$ and $\underline{\Theta}_2$ are determined by hand, by considering the coordinates of the points in the deformed and in the reference configurations. Each vector $\underline{\Theta}_i$ is defined by a single angle θ_i which is the rotation about a unit vector $\underline{e}_z$ directly perpendicular to $\underline{e}_x$ and $\underline{e}_y$. Thus $\underline{\Theta}_i = \theta_i \underline{e}_z$. θ_i can be regarded as the small change, when the system is loaded, of the initial orientation γ_i of the major axis of cylinder S_i; see Fig. 17 where this initial orientation γ_i is represented for each cylinder. Finally, it is worth noting that θ_i can be negative or positive, depending on the orientation of the rotation when the cylinders slightly move between the initial and deformed systems.

The relative displacement at the contact between S_2 and S_1 is denoted $\underline{U}_{S_2/S_1}$. Vector $\underline{U}_{S_2/S_1}$ is merely equal to the difference between $\underline{U}_{I_{S_2}}$ and $\underline{U}_{I_{S_1}}$, where I_{S_1} and I_{S_2} denote point I belonging to cylinders S_1 and S_2 respectively. Hence, $\underline{U}_{S_2/S_1} = \underline{U}_{I_{S_2}} - \underline{U}_{I_{S_1}}$. Vectors $\underline{U}_{I_{S_2}}$ and $\underline{U}_{I_{S_1}}$ can be deduced from both the displacement of the center of each cylinder and the rotation of these cylinders. Indeed, we have

$$\begin{cases} \underline{U}_{I_{S_1}} = \underline{U}_{O_1} + \underline{I_{S_1}O_1} \times \underline{\Theta}_1 \\ \underline{U}_{I_{S_2}} = \underline{U}_{O_2} + \underline{I_{S_2}O_2} \times \underline{\Theta}_2 \end{cases} \tag{4}$$

where symbol "$\times$" represents the cross product of two vectors. Thus

$$\underline{U}_{S_2/S_1} = \underline{U}_{O_2} - \underline{U}_{O_1} + \underline{I_{S_2}O_2} \times \underline{\Theta}_2 - \underline{I_{S_1}O_1} \times \underline{\Theta}_1 \tag{5}$$

The idea is now to distinguish between the normal and the tangential projection of this relative displacement. For this, it is necessary to know the components of a unit vector $\underline{t}$, which is tangent to both ellipses at point I.

Calculation of the tangent and normal vectors at the contact point. To find $\underline{t}$ and $\underline{n}$, we need to write the parametric equations of the ellipse modeling the border of S_i, $i = 1, 2$. The local coordinate system of each ellipse being defined by the axes going through its major and minor

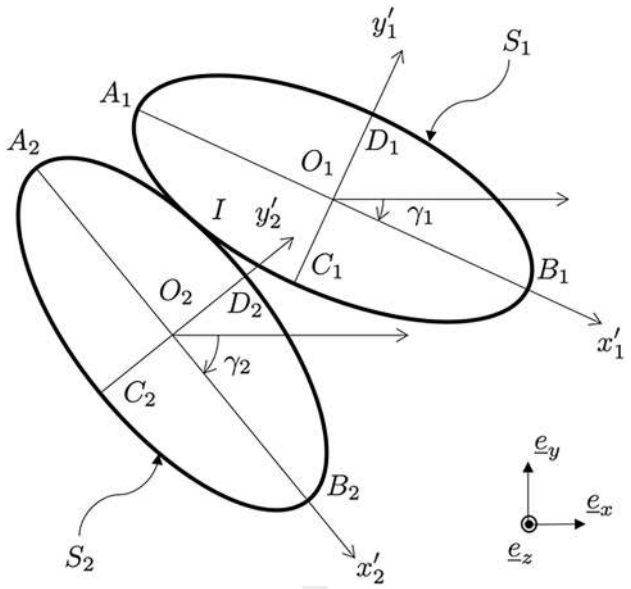

Fig. 17 Schematic view of the cross-sections of two cylinders in contact at point I

axes (see Fig. 17), the Cartesian equation of the ellipse can be written as follows in this local coordinate system:

$$\left(\frac{x'^2_i}{a'^2_i}\right) + \left(\frac{x'^2_i}{a'^2_i}\right) = 1 \tag{6}$$

where $2a_i = \|\underline{A_iB_i}\|$, $2b_i = \|\underline{C_iD_i}\|$ and x'_i and y'_i are the local coordinates of a point located on the ellipse defining the cross-section of S_i. The relationship between local and global coordinates writes as follows for each ellipse i:

$$\begin{pmatrix} x'_i \\ y'_i \end{pmatrix} = \begin{pmatrix} \cos\gamma_i & \sin\gamma_i \\ -\sin\gamma_i & \cos\gamma_i \end{pmatrix} \begin{pmatrix} x - x_{O_i} \\ y - y_{O_i} \end{pmatrix} \tag{7}$$

In the global coordinate system, Equation (6) becomes

$$\left(\frac{\left(\left(x - x_{O_i}\right)\cos\gamma_i - \left(y - y_{O_i}\right)\sin\gamma_i\right)^2}{a_i^2}\right) + \left(\frac{\left(-\left(x - x_{O_i}\right)\sin\gamma_i + \left(y - y_{O_i}\right)\cos\gamma_i\right)^2}{b_i^2}\right) = 1 \tag{8}$$

where x_{O_i} and y_{O_i} are the coordinates of the center O_i of each ellipse i. Finally, the parametric equations of each ellipse i are deduced with the following change of variables:

$$\begin{cases} \frac{x'_i}{a_i} = \frac{\left(x - x_{O_i}\right)\cos\gamma_i - \left(y - y_{O_i}\right)\sin\gamma_i}{a_i} = \cos\alpha \\ \frac{y'_i}{b_i} = \frac{-\left(x - x_{O_i}\right)\sin\gamma_i + \left(y - y_{O_i}\right)\cos\gamma_i}{b_i} = \sin\alpha \end{cases} \tag{9}$$

with $\alpha \in [0;2\pi]$. The coordinates of point I, namely x_I and y_I, are picked by hand in the global coordinate system. The value of α at point I, denoted by α_I, is therefore directly deduced from the following two equations, since all the quantities on the right side of both the equalities are known:

$$\begin{cases} \cos\alpha_I = \dfrac{\left(x_I - x_{O_i}\right)\cos\gamma_i - \left(y_I - y_{O_i}\right)\sin\gamma_i}{a_i} \\ \sin\alpha_I = \dfrac{-\left(x_I - x_{O_i}\right)\sin\gamma_i + \left(y_I - y_{O_i}\right)\cos\gamma_i}{b_i} \end{cases} \tag{10}$$

The objective is now to find the components of the tangent vector $\underline{t}$ in the local coordinate system i. These components are denoted $t_{x_i'}$ and $t_{y_i'}$. First the parametric equations of ellipse i can be written as follows in this local coordinate system:

$$\begin{cases} x_i' = a_i \cos\alpha \\ y_i' = b_i \sin\alpha \end{cases} \tag{11}$$

The components of the tangent vector $\underline{t}$ in the local basis are obtained by derivating Equation (11). This gives

$$\begin{cases} t_{x_i'} = -a_i \sin\alpha \\ t_{y_i'} = b_i \cos\alpha \end{cases} \tag{12}$$

These components must finally be expressed in the global coordinate system, which gives

$$\begin{pmatrix} t_{x_i} \\ t_{y_i} \end{pmatrix} = \begin{pmatrix} \cos\gamma_i & -\sin\gamma_i \\ \sin\gamma_i & \cos\gamma_i \end{pmatrix} \begin{pmatrix} t_{x_i'} \\ t_{y_i'} \end{pmatrix} \tag{13}$$

The components of vector $\underline{n}$, which is directly perpendicular to $\underline{t}$, are defined by

$$\begin{cases} n_{x_i} = t_{y_i} \\ n_{y_i} = -t_{x_i} \end{cases} \tag{14}$$

The components of $\underline{t}$ and $\underline{n}$ at point I are simply obtained by feeding Equation (12) above with α_I found with Equation (10) and then applying Equations (13) and (14) in this particular case. It should be checked that vector $\underline{n}$ is correctly oriented, *i.e.* outwards.

Remark Each cylinder i should provide its own vector $\underline{t}$. For a given contact, two cylinders being involved, it should be verified that these two versions of the same tangent vector are close to each other. The mean vector should be retained for the following and final calculations proposed in Equation (15). The same remark holds for $\underline{n}$.

Final estimation of interpenetration and sliding between ellipses. $\underline{n}$ and $\underline{t}$ being defined at point I, the amplitude of the sliding *sld* of S_2 on S_1 can be obtained by projecting $\underline{U}_{S_2/S_1}$ defined in Equation (5) on vector $\underline{t}$ calculated at point I, and the interpenetration *int* of S_2 in S_1 by projecting $\underline{U}_{S_2/S_1}$ on vector $\underline{n}$ calculated at point I. These two quantities are equal to:

$$\begin{cases} sld = \underline{U}_{S_2/S_1} \cdot \underline{t} \\ int = -min\left(\underline{U}_{S_2/S_1} \cdot \underline{n}, 0\right) \end{cases} \tag{15}$$

where "·" represents the dot product of two vectors. In Equation (15) above, $\underline{n}$ should have the same orientation of vector $\underline{O_1O_2}$ to consider that interpenetration occurs only if the projection of $\underline{U}_{S_2/S_1}$ onto $\underline{n}$ is negative. If this projection is positive, it means that S_2 and S_1 are no longer in contact after loading the system, so no interpenetration occurs and $int = 0$. Concerning *sld*, it is worth mentioning that its absolute value should be considered for comparison purposes with mechanical dissipation, which is a positive calorific quantity.

The procedure above should be applied to each cylinder of the system and to each contact point between this cylinder and its neighbors.

Acknowledgements K. Jongchansitto acknowledges the National Research Council of Thailand (NRCT) through the Royal Golden Jubilee Ph.D. program (grant no. PHD/0100/2561) for the support during this research. X. Balandraud acknowledges the Région Auvergne-Rhônes-Alpes for the support in this study (Project: IRICE Fabrication additive, number: 18 009727 01-59941, operation: P088O005). The authors would like to thank Mr. Alexis Gravier and Mr. Clément Weigel, Sigma Clermont engineering school, for setting up the experimental mechanical device.

Data Availability The datasets obtained during and/or analyzed during the current study are available from the corresponding author on reasonable request.

Declarations

Conflicts of Interests The authors declare no competing of interest.

References

1. Jaeger HM (2005) Sand, jams and jets. Phys World 18:34–39
2. Jaeger HM, Nagel SR, Behringer RP (1996) Granular solids, liquids, and gases. Rev Mod Phys 68:1259–1273
3. Eltawahni HA, Yu AB (2019) Powder Processing: Models and Simulations. Reference Module in Materials Science and Materials Engineering, Elsevier. https://doi.org/10.1016/B978-0-12-803581-8.11651-0
4. Radjai F, Roux JN, Daouadji A (2017) Modeling granular materials: century-long research across scales. J Eng Mech 143:04017002
5. Khalili MH, Brisard S, Bornert M, Aimedieu P, Pereira JM, Roux JN (2017) Discrete digital projections correlation: a reconstruction-free method to quantify local kinematics in granular media by X-ray tomography. Exp Mech 57:819–830
6. Mueth DM, Jaeger HM, Nagel SR (1998) Force distribution in a granular medium. Phys Rev E 57:3164–3169
7. Schneebeli G (1956) Une analogie mécanique pour les terres sans cohésion. C R Acad Sci 243:125–126

8. Calvetti F, Combe G, Lanier J (1997) Experimental micromechanical analysis of a 2D granular material: Relation between structure evolution and loading path. Mech Cohes-Frict Mat 2:121–163
9. Misra A, Jiang H (1997) Measured kinematic fields in the biaxial shear of granular materials. Comput Geotech 20:267–285
10. Slominski C, Niedostatkiewicz M, Tejchman J (2007) Application of particle image velocimetry (PIV) for deformation measurement during granular silo flow. Powder Techn 173:1–18
11. Hall SA, Wood DM, Ibraim E, Viggiani G (2010) Localised deformation patterning in 2D granular materials revealed by digital image correlation. Granular Matter 12:1–14
12. Richefeu V, Combe G, Viggiani G (2012) An experimental assessment of displacement fluctuations in a 2D granular material subjected to shear. Geotechnique Lett 2:113–118
13. Marteau E, Andrade JE (2017) A novel experimental device for investigating the multiscale behavior of granular materials under shear. Granular Matter 19:77
14. Hurley R, Marteau E, Ravichandran G, Andrade JE (2014) Extracting inter-particle forces in opaque granular materials: Beyond photoelasticity. J Mech Phys Solids 63:154–166
15. Hurley RC, Lim KW, Ravichandran G, Andrade JE (2016) Dynamic inter-particle force inference in granular materials: method and application. Exp Mech 56:217–229
16. Karanjgaokar N (2017) Evaluation of energy contributions using inter-particle forces in granular materials under impact loading. Granular Matter 19:36
17. Shukla A, Damania C (1987) Experimental investigation of wave velocity and dynamic contact stresses in an assembly of disks. Exp Mech 27:268–281
18. Roessig KM, Foster JC, Bardenhagen SG (2002) Dynamic stress chain formation in a two-dimensional particle bed. Exp Mech 42:329–337
19. Mirbagheri SA, Ceniceros E, Jabbarzadeh M, McCormick Z, Fu HC (2015) Sensitively photoelastic biocompatible gelatin spheres for investigation of locomotion in granular media. Exp Mech 55:427–438
20. Barés J, Cárdenas-Barrantes M, Cantor D, Renouf M, Azéma E (2022) Softer than soft: Diving into squishy granular matter. Pap Phys 14:140009
21. Cárdenas-Barrantes M, Barés J, Renouf M, Azéma E (2022) Experimental validation of a micromechanically based compaction law for mixtures of soft and hard grains. Phys Rev E 106:L022901
22. Cantor D, Cardenas-Barrantes M, Preechawuttipong I, Renouf M, Azema E (2020) Compaction model for highly deformable particle assemblies. Phys Rev Let 124:208003
23. Batsale J, Chrysochoos A, Pron H, Wattrisse B (2012) Thermographic analysis of material behavior. In: Grédiac M, Hild F (eds) Full-field measurements and identification in solid mechanics, vol 16. Wiley, Hoboken, pp 439–468
24. Dulieu-Barton JM (2012) Thermoelastic Stress Analysis. In: P.K. Rastogi, E. Hack (eds) Optical methods for solid mechanics: a full-field Approach. Chapter 8. Wiley-VCH, Weinheim
25. Germain P, Nguyen QS, Suquet P (1983) Continuum thermodynamics J Appl Mech 50:1010–1020
26. Halphen B, Nguyen QS (1975) Sur les matériaux standards généralisés. J de Mec 14:39–63
27. Luong MP (1982) Détection par thermographie infrarouge du seuil caractéristique d'un sable cisaillé en vibrations. Comptes Rendus Acad Sc Serie II(295):87–90
28. Luong MP (1986) Characteristic threshold and infrared vibrothermography of sand. Geotech Test J 9:80–86
29. Luong MP (2001) Infrared thermography of the dissipative behaviour of sand, In: Proceedings of the fifteenth International Conference on Soil Mechanics and Foundation Engineering Vols 1–3, Istanbul, Turkey, August 27–31, 2001. A.A. Balkema Publishers, Leiden, Netherlands, pp. 199–202
30. Luong MP (2007) Introducing infrared thermography in soil dynamics. Infrared Phys Technol 49:306–311
31. Jongchansitto P, Balandraud X, Grédiac M, Beitone C, Preechawuttipong I (2014) Using infrared thermography to study hydrostatic stress networks in granular materials. Soft Matter 10:8603–8607
32. Chaiamarit C, Balandraud X, Preechawuttipong I, Grédiac M (2015) Stress network analysis of 2D non-cohesive polydisperse granular materials using infrared thermography. Exp Mech 39:761–769
33. Jongchansitto P, Balandraud X, Preechawuttipong I, Le Cam J-B, Garnier P (2018) Thermoelastic couplings and interparticle friction evidenced by infrared thermography in granular materials. Exp Mech 58:1469–1478
34. Hopzapfel GA (2000) Nonlinear Solid Mechanics - A Continuum Approach for Engineering. John Wiley & Son, New York
35. Gough J (1805) A description of a property of Caoutchouc or India Rubber. Proc Lit Phil Soc 1:288–295
36. Joule JP (1857) On some thermodynamic properties of solids. Phil Mag 4th 14:227
37. Le Cam JB, Samaca Martinez JR, Balandraud X, Toussaint E, Caillard J (2015) Thermomechanical analysis of the singular behavior of rubber: entropic elasticity, reinforcement by fillers, strain-Induced crystallization and the Mullins effect. Exp Mech 55:771–782
38. Pichon P (2010) Fatigue thermomécanique des élastomères polyurethane : caractérisation expérimentale de l'évolution des microstructures et modélisation des échanges thermiques. PhD thesis report, Institut National des Sciences Appliquées de Lyon, p. 136 (in French)
39. Chrysochoos A, Peyroux R (1998) Experimental analysis and numerical simulation of thermomechanical couplings in solid materials. Rev Gen Therm 37:582–606
40. Chrysochoos A, Louche H (2000) An infrared image processing to analyse the calorific effects accompanying strain localisation. Int J Eng Sci 38:1759–1788
41. Douellou C, Balandraud X, Duc E (2022) Fatigue characterization by heat source reconstruction under continuously varying stress amplitude. Int J Fatigue 159:106782
42. Popov VL (2010) Rigorous Treatment of Contact Problems – Hertzian Contact. In: Contact Mechanics and Friction. Physical Principle and applications. Springer Berlin, Heidelberg, pp 55–70. https://doi.org/10.1007/978-3-642-10803-7